

<https://doi.org/10.1038/s42003-025-08364-6>

Computational loop reconstruction based design of efficient PET hydrolases

Check for updates

Hongzhao Wang^{1,6}, Yuntao Cun^{1,6}, Minxuan Wang^{1,2,6}, Xiaoyu Du^{3,6}, Zhenwu Yang¹, Hao Wang^{①,3}, Jun Zhang⁴, Pengyu Wang⁴, Yue Feng^{①,3} & Yushan Zhu^{①,5}

Enzymatic PET depolymerization represents a promising approach for establishing a circular economy for PET plastics. Nonetheless, limitations in enzyme activity persist as significant challenges to its industrial application. In this research, the backbone structure of the β 6- β 7 loop for PET hydrolase Bhr-PETase derived from the *thermophilic bacterium* HR29 was reconstructed by introducing double mutations (H218N/F222M), resulting in variant Bhr-NMT with high thermal stability ($T_m = 92.9$ °C) and 87% increase in activity. Moreover, the loop reconstruction mutations are transplanted into the engineered PET hydrolases LCC-ICCG and Kubu-P^{M12}, resulting variants LCC-ICCG-NM ($T_m = 92.4$ °C) and Kubu-P^{M12}-NM ($T_m = 92.9$ °C). Under high substrate concentration (165 g kg⁻¹) and an enzyme loading of 0.5 mg_{enzyme} g_{PET}⁻¹, the designed variants Bhr-NMT, LCC-ICCG-NM, and Kubu-P^{M12}-NM achieve an overall conversion of 93%, 90%, and 94%, respectively, outperforming the benchmark LCC-ICCG (85%). Notably, under reduced enzyme loading (0.3 mg_{enzyme} g_{PET}⁻¹), Kubu-P^{M12}-NM still reaches an overall conversion of 91%, which is significantly superior to benchmarks Kubu-P^{M12} (83%) and LCC-ICCG (71%). Overall, the engineered PET hydrolases demonstrate significant potential for industrial PET waste recycling.

Plastics, prized for their thermal resistance, mechanical strength, and chemical stability, are extensively used worldwide; however, only ~9% are recycled¹. Among these materials, polyethylene terephthalate (PET) stands out as one of the most widely produced synthetic polyesters, with an annual production volume exceeding 82 million tons^{2,3}. However, the inherent chemical recalcitrance of PET contributes to its persistence in the environment, leading to accumulation in oceans, soils, and even the food chain, thus posing serious ecological threats^{4,5}. In response, global initiatives to advance PET depolymerization technologies are focused on promoting a sustainable circular economy for this material^{6,7}.

Compared to chemical degradation methods^{8,9}, enzymatic PET depolymerization operates under milder reaction conditions and yields purer products, which facilitates PET recycling and promotes its industrial applications^{2,10-12}. In 2005, Müller et al. discovered that after incubating at 55 °C for three weeks, the cutinase TfH derived from *Thermobifida fusca* could degrade PET films by up to 17 μm, resulting in a weight loss of 54%¹³. To accelerate the enzymatic PET degradation, reactions should be conducted near PET's glass transition temperature (T_g , 65–71 °C)^{14,15}. At this

temperature, increased mobility in the amorphous regions of PET improves enzyme-PET binding¹⁶⁻¹⁸. Consequently, PET hydrolases must exhibit high thermal stability¹⁹ for industrial applications. Some cutinases isolated from thermophilic species can operate under moderate to high temperatures without modification¹⁹⁻²³, showing promising potential for further engineering. Over the past 20 years, several cutinase variants have been developed, significantly improving the thermal stability and catalytic efficiency^{19,24-29}. A breakthrough was achieved in 2020 when Tournier et al. engineered the variant LCC-ICCG, which degraded over 90% of PET within 10 h under industrial conditions, demonstrating the best productivity-to-enzyme cost ratio among PET hydrolases²⁷. Bhr-PETase, identified from the metagenome of thermophilic bacterium HR29³⁰, belongs to the cutinase family and exhibits superior structural stability with a melting temperature (T_m) of 95.6 °C, representing the highest thermal stability among PET hydrolases identified in nature. Furthermore, Bhr-PETase displays higher PET hydrolytic activity at the T_g of PET compared to other cutinases^{28,31}, thereby making it a promising template for protein engineering. In 2024, Wu et al. redesigned an activity-enhancing variant of Bhr-PETase

¹College of Life Science and Technology, Beijing University of Chemical Technology, Beijing, China. ²PetroChina Petrochemical Research Institute, China National Petroleum Corporation (CNPC), Beijing, China. ³Beijing Advanced Innovation Center for Soft Matter Science and Engineering, State Key Laboratory of Chemical Resource Engineering, Beijing University of Chemical Technology, Beijing, China. ⁴Department of Chemical Engineering, Tsinghua University, Beijing, China.

⁵State Key Laboratory of Green Biomanufacturing, Beijing University of Chemical Technology, Beijing, China. ⁶These authors contributed equally: Hongzhao Wang, Yuntao Cun, Minxuan Wang, Xiaoyu Du. e-mail: fengyue@mail.buct.edu.cn; zhuys@mail.buct.edu.cn

(TurboPETase, $T_m = 84^\circ\text{C}$), which could nearly completely degrade PET within 8 h under industrial conditions at 65°C ³¹. Although engineered cutinases have sufficient thermal stability, their limited activity requires large enzyme quantities^{19,27,31,32} to achieve a 90% conversion at high PET concentration levels (>15% w/v), constraining the economic feasibility of enzymatic PET recycling for industrial applications³³.

Enzymatic hydrolysis of PET is an interfacial catalytic process that occurs at the solid-liquid interface³⁴. In 1967, Flory et al. discovered that amorphous PET exhibits a unique structural configuration³⁵. In 1998, Schmidt-Rohr et al. characterized the chain conformations of PET in the glassy state using two-dimensional double-quantum nuclear magnetic resonance (NMR), revealing that in amorphous PET, the gauche conformation accounted for 86%³⁶. In 2016, Oda et al. discovered a PET hydrolase, IsPETase ($T_m = 46^\circ\text{C}$), from a new bacterium, *Ideonella sakaiensis* 201-F6³⁷, which exhibits a higher substrate preference for amorphous PET, with a binding pocket structure that aligns more closely with the gauche conformation. Guo et al. analyzed the crystal structures of IsPETase, revealing that the tryptophan residue located in the $\beta 6-\beta 7$ loop displays distinct conformational states³⁸⁻⁴⁰. Assuming IsPETase could remain stable at 70°C , its activity would likely exceed that of other PET hydrolases, which has led to the discovery of numerous IsPETase variants with enhanced thermal stability^{30,41-44}. Even with a T_m increase of 36.5°C over the wild type, the most thermally stable IsPETase variant, HOT-PETase, still cannot maintain prolonged activity at PET's glass transition temperature (T_g)⁴⁴.

The enhanced catalytic efficiency of PET hydrolases enables shorter reaction time and higher productivity, thereby optimizing the economics of large-scale enzymatic PET depolymerization. In this study, we developed a computational strategy to redesign the scaffold structure of PET hydrolases tailored to the structural characteristics of amorphous PET. Utilizing the highly stable Bhr-PETase, LCC-ICCG²⁷, and Kubu-P^{M12}⁴⁵ as templates, we obtained variants with comparable thermal stability and significantly enhanced catalytic activity.

Results

Polymer structural characteristics guided computational redesign of PET hydrolase

The cleavage mechanism of PET polymer chains can be categorized into exo-type and endo-type processes⁴⁶. The computational redesign model for PET hydrolases developed here focuses on the endo-type degradation of amorphous PET. The template selected for redesigning was Bhr-PETase ($T_m = 95.6^\circ\text{C}$), which was derived from the *thermophilic bacterium HR29*, and its crystal structure was taken directly from the Protein Data Bank (PDB ID: 7EOA). Our enzyme design strategy focuses on enhancing catalytic activity by lowering the activation energy barrier of the transition state (TS) complex formed between the PET model substrate and the enzyme^{47,48}. The catalytic mechanism of PET hydrolases follows the classical four-step serine hydrolase pathway (Fig. 1b), and both the acylation and deacylation processes require a higher activation energy barrier⁴⁹. A QM/MM molecular dynamics simulations study on the PET hydrolase revealed that acylation is the rate-limiting step, with the acylation transition state (TS1, Fig. 1b) exhibiting the highest activation energy barrier⁵⁰. Therefore, in this study, the structure of TS1 was utilized to construct a computational model for enzyme redesign, with the internal coordinates of the atoms in the tetrahedral intermediate derived from the calculations conducted by Moliner et al.⁴⁹. The redesign of the PET hydrolase was performed using the computational enzyme design tool PRODA developed in our laboratory^{47,48,51-53}.

To reflect the structural characteristics of amorphous PET polymers and their translational, rotational, and conformational degrees of freedom within the active site of the enzyme, a model substrate (Fig. 1a) composed of three PET monomers was constructed in accordance with the placement rules derived from MD simulations and quantum chemical calculations by Boyd et al. (Table S1)^{16,54}. The torsion angles of the four critical bonds (Fig. 1a) in the PET chain were defined as follows. (1) Bond I (CA-CD-O-C),

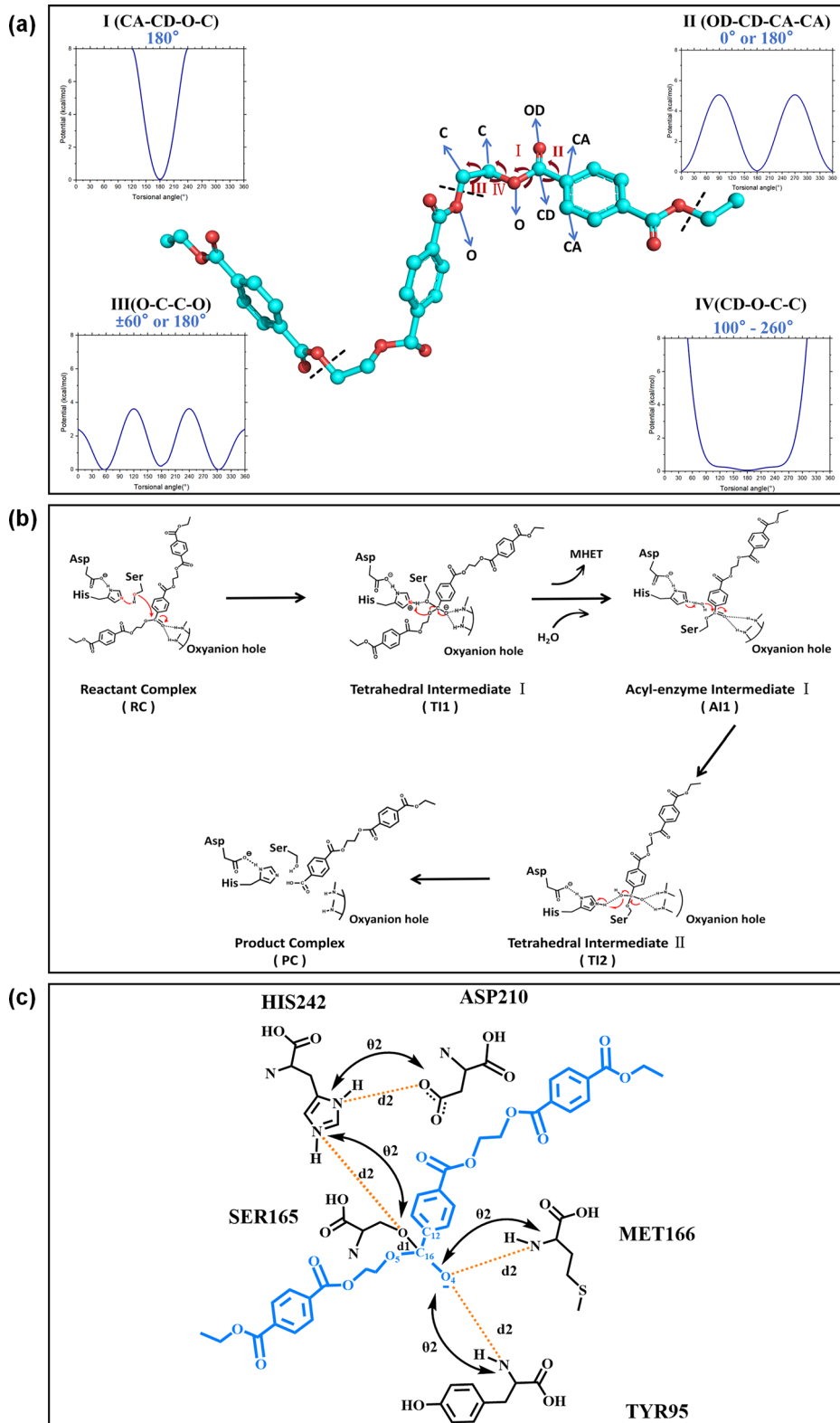
which links ethylene glycol to the ester bond, has a dihedral angle set at 180° . (2) Bond II (OD-CD-CA-CA), connecting the phenyl group to the ester bond, can have dihedral angles of either 0° or 180° . (3) Bond III (O-C-C-O), the ethylenic bond, has dihedral angles that range from 65° to 75° or from -75° to -65° . (4) Bond IV (CD-O-C-C), the glycol linkage, exhibits dihedral angles between 100° and 260° . Considering the catalytic geometric constraints (Fig. 1c and Table S2), 176,455 conformations were generated using a previously developed small molecule placement tool⁴⁸. To ensure the diversity of these conformations, a filter was applied based on a root-mean-square deviation (RMSD) threshold of 0.3 \AA , resulting in a rotamer library of the TS with 4526 conformations.

Our enzyme redesign principle was to enhance the binding affinity between the PET substrate and the active site⁵⁵. All residues within 10 \AA of the substrate were selected as design sites (Table S13), where the amino acids at 11 sequence change positions (G94, Y95, T96, A97, S101, H164, M166, W190, F243, N246, S247) were varied among (YACFILMNQSVWGH). In addition, 26 positions, including catalytic triads (S165/H242/D210), surrounding the binding pocket, were subjected to side-chain conformational optimization. The geometric constraints between the TS and catalytic residues and the positions of redesigned sites relative to the substrate are shown in Figs. 1c, 2a, respectively. Sequence optimization was performed using the enzyme design tool PRODA^{47,48}, generating 80 sequences with single mutation. Among these, 11 sequences exhibited binding energy lower than that of the wild type, and 64 sequences showed reduced Van der Waals repulsion with the TS compared to the wild type. More details of the designed variants are presented in Table S3.

To eliminate false-positive sequences predicted by the energy calculations, 56 sequences underwent dynamic evaluation using high-throughput MD simulations^{52,56}. The criteria for sequence selection were: (1) the calculated binding energy change $\Delta\Delta G_{\text{bind}} < 0 \text{ kcal/mol}$ or the total energy change $\Delta\Delta G_{\text{total}}$ ranked in the top 40 among all sequences; (2) the Van der Waals repulsion change $\Delta\Delta G_{\text{VDW-repulsion}} < 0 \text{ kcal/mol}$; (3) diversity of mutations; (4) inspection of the computed binding geometries. To evaluate each sequence within the extensive MD simulation data, we developed four catalytic indicators based on the mechanism of serine hydrolases, including the RMSD of the TS, the nucleophilic attack distance, and the stability of the two oxyanion hole hydrogen bonds. The four catalytic indicators were calculated as the averages of $10 \times 1 \text{ ns}$ MD simulations, with the results presented in Fig. 2b, c, and Table S4. More than 50% of the sequences (30/56) appeared in the first quadrant of both Fig. 2b, c, indicating that these sequences outperformed the wild type in all four catalytic indicators. Eight sequences were ultimately selected for experimental validation based on the results from the energy calculations and the MD simulations. The selection criteria included the following: (1) all four catalytic indicators were superior to those of the wild-type; (2) $\Delta\Delta G_{\text{VDW-repulsion}} < 0 \text{ kcal/mol}$; (3) diversity of mutations; (4) inspection of the binding conformations in the trajectories of MD simulations.

The PET depolymerization activities of the variants were evaluated utilizing bottle-grade post-consumer PET (Pc-PET) powder. All variants were assessed at a substrate concentration of 0.16% (w/v), and the reactions were conducted with an enzyme loading of $1 \text{ mg}_{\text{enzyme}} \text{ g}_{\text{PET}}^{-1}$ at 68°C for 12 h. In addition, the thermal stability of the variants was evaluated by nano-differential scanning fluorimetry (NanoDSF). The activities and T_m values of the variants were presented in Fig. 2d and Tables S8 and S9. The activities of variant M1 (F243T, $T_m = 95.9^\circ\text{C}$) and M2 (F243I, $T_m = 95.6^\circ\text{C}$) were 1.34 and 1.11 times greater than the corresponding values of the wild type, respectively, consistent with the calculation results. In variants M1 and M2, the Van der Waals repulsion between the residue at position 243 and the PET decreased from 11.61 kcal/mol in the wild-type to 0 kcal/mol (Fig. S1a, b), indicating that in the template Bhr-PETase, the Van der Waals repulsion between the residue F243 and PET are primarily caused by the side chain atoms rather than the backbone atoms. Because of the enhanced thermal stability and activity exhibited by variant M1, it was chosen as a new template for further design.

Fig. 1 | Structural characteristics of amorphous PET polymer, catalytic mechanism of PET hydrolase, and computational model for the redesign of PET hydrolase. a Structural characteristics of amorphous PET polymer and the potential energy variations of each torsion angle in the PET polymer chain. The molecular simulation results were obtained from Boyd et al.¹⁶. Type I bond (CA-CD-O-C) linking ethylene glycol and the ester, its minimum potential energy angle lies at 180°; type II bond (OD-CD-CA-CA) linking phenyl and the ester, its minimum potential energy angle lies at 0° or 180°; type III bond (O-C-C-O), the ethylenic bond, its minimum potential energy angle lies at ±60° or 180°; type IV bond (CD-O-C-C), the glycol bond, its low potential energy angle lies in the range of 100°–260°. b Catalytic mechanism of PET hydrolase. The reaction initiates with a nucleophilic attack by serine on the polymer's ester bond, forming the first tetrahedral intermediate (T11). Then the first reaction product (MHET or an oligomer) was released, forming an acyl-enzyme intermediate (Al). Subsequently, a water molecule attacks the new ester bond in Al, resulting in deacylation and the formation of a second tetrahedral intermediate (T12), ultimately releasing the PET fragment. The red arrows indicate the electron transfer pathways. c Computational enzyme design model and the catalytic geometric constraints. The PET model substrate is marked in blue, while the catalytic triad and oxyanion hole residues are shown in black. d₂ represents the hydrogen bond distance constraint between the donor atom and the acceptor atom (2.6–3.2 Å). θ₂ represents the hydrogen bond angle constraint between the donor, the hydrogen atom, and the acceptor (120–180°). d₁ represents the nucleophilic attack distance constraint of the hydroxyl oxygen of serine and the central carbon atom of the substrate ((Ser) OG-C12 (PET), 1.4–1.7 Å).



Loop reconstruction based computational enzyme redesign

Although the PET degradation activity of variant M1 was promoted, we observed that there still exists serious Van der Waals repulsion between the backbone of the β6-β7 loop and PET (Fig. 2e). Therefore, our further design objective was to enhance the compatibility of the β6-β7 loop with the dominant conformation of amorphous PET through the following two steps: (1) remodeling the loop to identify a backbone structure that

minimizes the Van der Waals repulsion with PET; (2) performing sequence optimization to find sequences capable of folding into the remodeled structure. The β6-β7 loop (L187-T195) was remodeled using the protein modeling tool Modeler¹⁸, yielding a total of 50 distinct conformations (Fig. 3a). Subsequently, the generated rotamer library for PET model substrate was employed to conduct recapitulation⁵⁷ calculations of the enzyme-PET complexes for each of the 50 conformations (Fig. S2 and

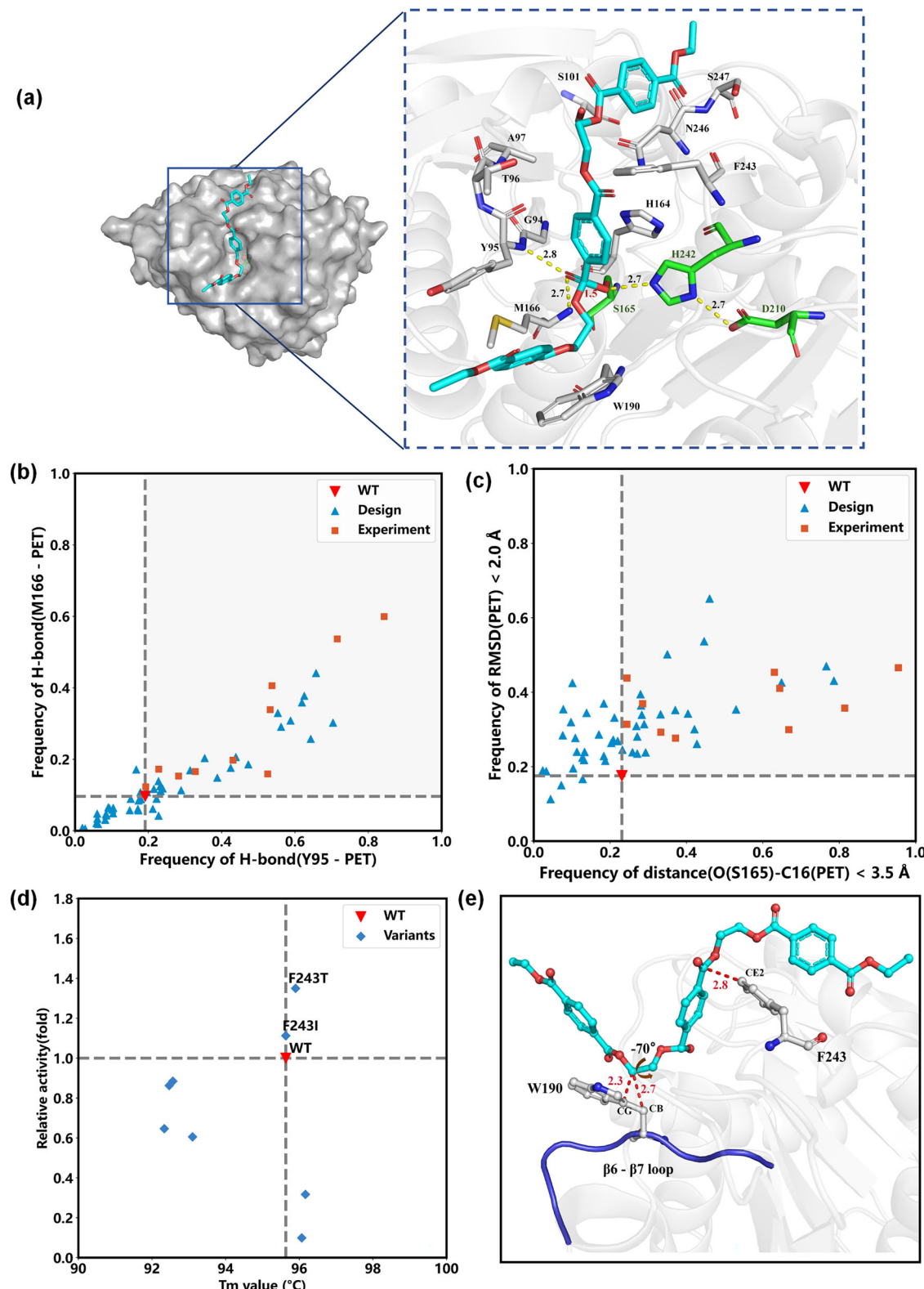


Table S5). Among the 17 remodeled loops, the Van der Waals repulsion between the residue W190 in the β_6 - β_7 loop and PET is lower than that of the wild type (Fig. S2), but seven conformations exhibit folding energies exceeding 100 kcal/mol, indicating significant structural inconsistencies. For the remaining ten conformations, 5×5 ns MD simulations were conducted for further validation. The distribution of Van der Waals repulsion between the backbone atoms of residue W190 and the PET was

calculated to evaluate these conformations (Fig. S4a). Details of the MD simulations method are shown in the supporting information (Fig. S3). Loop10 exhibits the lowest and most concentrated Van der Waals repulsion distribution (Fig. S4a), with a significant reduction in Van der Waals repulsion compared to the wild-type crystal structure (Fig. S4b).

The binding energy between the remodeled Loop10 and PET is enhanced by 17.47 kcal/mol compared to the wild-type crystal structure

Fig. 2 | Computational redesign of the PET hydrolase Bhr-PETase and experimental characterization of the designed variants. **a** Design sites of PET hydrolase Bhr-PETase. In the left image, the PET model substrate is shown in a stick model, while the catalytic residue S165 is marked with a ball-and-stick model. In the right image for enlarged view, the catalytic triad residues (S165/H242/D210) are colored in green, and the amino acid type change residues are colored in gray. The hydrogen bonds are shown in dashed lines colored in yellow, around which the numbers indicate the hydrogen bond distances (\AA). **b, c** Catalytic indicators calculated from the high-throughput MD simulations ($10 \times 1 \text{ ns}$) for the designed variants. The blue triangles represent the computationally designed variants, while the orange squares represent the experimentally evaluated variants. **b** The abscissa represents the probability of hydrogen bonding between oxyanion hole residue Y95 and the PET model substrate, and the ordinate represents the probability of hydrogen bonding between oxyanion hole residue M166 and the PET model substrate. The hydrogen bonding criteria used for catalytic indicators are: the bond length (donor-acceptor) $< 3.5 \text{ \AA}$, and the bond angle (donor-H-acceptor) $> 120^\circ$. **c** The abscissa represents the probability of the nucleophilic attack distance ((S165) OG-C16 (PET)) being less

than 3.5 \AA , and the ordinate represents the probability of the RMSD of the PET model substrate is less than 2.0 \AA . **d** Catalytic activity and thermal stability evaluation of the designed variants. The ordinate represents the ratio of PET conversion for the variants compared to that of the wild-type. Each variant was tested at a temperature of 68°C for 12 h, using 0.16% (w/v) of P_c-PET powder and $1 \text{ mg}_{\text{enzyme}} \text{ g}_{\text{PET}}^{-1}$ of enzyme in 100 mM phosphate buffer (pH 8.0). The T_m values of the variants were measured using the DSF method, in which the samples were heated from 25°C to 110°C at a rate of 2°C min^{-1} . All reactions were carried out in triplicate. **e** Computed binding geometries of PET model substrate and the wild-type Bhr-PETase based on the crystal structure (PDB ID: 7EOA). The Van der Waals repulsion between two atoms is shown in dashed lines colored in red, around which the numbers indicate the distances (\AA). The β_6 - β_7 loop is shown in the purple cartoon model. In Bhr-PETase, the closest distances from the side chain and backbone of residue W190 to PET model substrate are 2.3 \AA ((W190) CG-C18 (PET)) and 2.7 \AA ((W190) CB-C18 (PET)), respectively. The closest distance of residue F243 to PET model substrate is 2.8 \AA ((F243) CE2-O7 (PET)).

(PDB ID: 7EOA), primarily due to a reduction in Van der Waals repulsion between residue W190 and PET from 26.71 to 13.61 kcal/mol. Additionally, the closest distance between the PET and the backbone atoms of residue W190 increased from 2.7 to 4.2 \AA (Fig. 3b). Notably, compared to the wild type, the folding energy of Loop10 increased from -134.17 kcal/mol to 6.29 kcal/mol , indicating significant steric clashes between residues in the β_6 - β_7 loop and surrounding residues that prevent the current sequence from folding into the intended remodeled conformation. Therefore, redesign of the β_6 - β_7 loop and adjacent residues is necessary to optimize interactions among these residues.

A computational model for the redesign of the β_6 - β_7 loop was constructed based on the structure of Loop10 and the generated rotamer library for the PET model substrate. The design strategy for this section is to reduce the folding energy of the sequence while maintaining its binding energy, ensuring that the mutations enhance activity without negatively impacting the thermal stability of the variant. All residues within 10 \AA of the residue W190 and 7 \AA of the TS were selected as design sites, where the amino acids at nine sequence change positions (T136, L137, H156, T157, F161, I169, V177, H183, and F187) were varied among (YACFILMNQSVWGH). Among these residues, the remaining 24 residues were subjected to side-chain conformational optimization. Based on the beneficial mutation F243T (M1), sequence optimization calculations were performed using our enzyme design tool PRODA^{47,48}, resulting in 49 sequences with double mutations (Table S6). To eliminate false-positive sequences and ensure the diversity of mutations, high-throughput MD simulations were conducted on all generated sequences ($10 \times 1 \text{ ns}$ MD simulations). Four catalytic indicators were calculated for each sequence (Fig. 3c, d, and Table S7), and ten sequences were selected for experimental validation. The selection criteria were: (1) all four catalytic indicators were superior to those of M1; (2) the folding energy of the variants was lower than that of M1; (3) diversity of mutations; (4) inspection of the binding conformations in the trajectories of MD simulations.

The activity and thermal stability of the ten variants were experimentally evaluated, with the results presented in Fig. 3g and Tables S8 and S9. The T_m values of the variants M12 (F222I/F243T) and M10 (F222M/F243T) increased by 0.9°C and 2.4°C , respectively, compared to M1, although their activities decreased by 12.79% and 8.21%, respectively. In contrast, variant M9 (H218A/F243T) exhibited a 3% increase in activity relative to M1, but its T_m value decreased significantly by 13.1°C . Mutations in M9, M10, and M12 were concentrated at the 218 and 222 positions, while mutations at other positions exhibited substantial decreases in both activity and T_m compared to M1. Consequently, a redesign of synergistic mutations at positions 218 and 222 was performed, resulting in the 102 sequences with triple mutations via sequence optimization calculations using the PRODA^{47,48}, all of these sequences exhibited folding energies lower than that of M1 (Table S6). High-throughput MD simulations were conducted on all 102 sequences, and four catalytic indicators were calculated to evaluate their

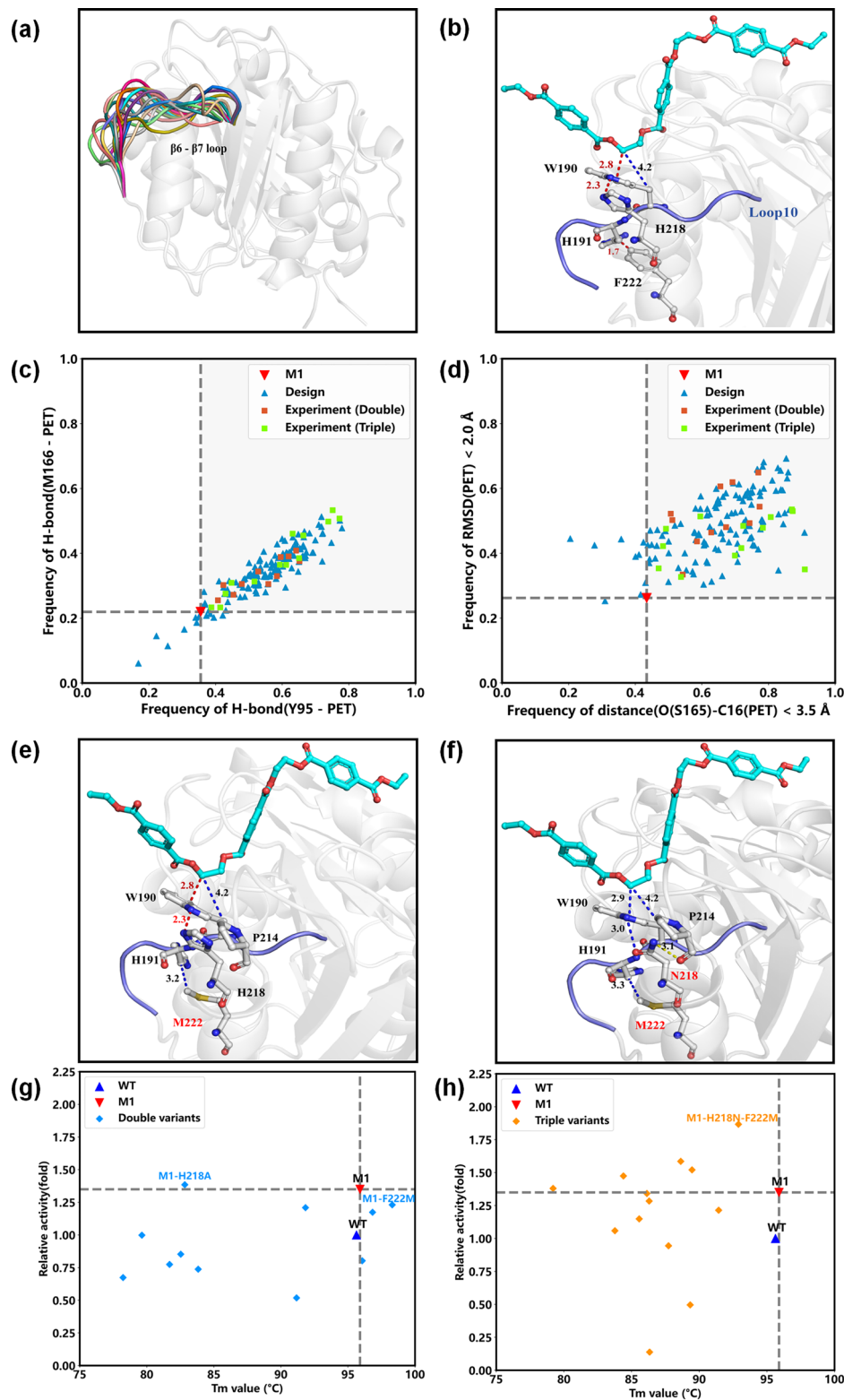
catalytic performance (Fig. 3c, d). Based on the criteria outlined in the preceding paragraph, 13 sequences were selected for experimental validation.

The experimental evaluations of activity and thermal stability for 13 variants are presented in Fig. 3h and Tables S8, and S9. Among these, five variants exhibited higher activity than M1, i.e., M20 (H218N/F222M/F243T, Fig. 3f), M21 (H218V/F222M/F243T), M22 (H218L/F222I/F243T), M23 (H218S/F222M/F243T), and M24 (H218S/F222L/F243T), with their activities being 1.87, 1.59, 1.52, 1.48, and 1.38 times greater than the wild-type, respectively. Analysis of the free energy of residues surrounding the β_6 - β_7 loop revealed significant clashes between residue F222 and adjacent residues L172, H191, and I204 ($\Delta G_{\text{VDW-repulsion}} > 6.5 \text{ kcal/mol}$) (Fig. 3b). The mutation of phenylalanine to the more flexible methionine on position 222 promotes better hydrophobic packing between the residue M222 and the adjacent residues L172 and H191 (Fig. 3e), thereby enhancing the thermal stability of the enzyme. In the structure of Loop10, the Van der Waals repulsion between residues H218 and W190 is calculated at 8.54 kcal/mol (Fig. 3b), while that between their backbone atoms is 0 kcal/mol , indicating that the rigidity of the imidazole group in H218 restricts the rotation of the side chain in W190 and indirectly hinders the binding of PET to the enzyme. The mutation of the histidine to smaller side chain amino acids (serine, alanine, threonine, asparagine, and leucine) resulted in a reduction of the Van der Waals repulsion with W190, thereby enhancing the enzyme's activity.

Experimental assessment of highly active variant under industrial conditions

Among the variants designed based on loop reconstruction, M20 (Bhr-NMT) exhibited the highest PET depolymerization activity while maintaining thermal stability ($T_m = 92.4^\circ\text{C}$) comparable to the wild-type. To further investigate the feasibility of applying Bhr-NMT under industrial conditions, a series of experimental evaluations were conducted. First, the PET hydrolytic activities of Bhr-NMT and the well-known engineered PET hydrolase LCC-ICCG²⁷ were compared over a temperature range of 50°C - 80°C (Fig. 4a). As the reaction temperature (68°C , 72°C , and 75°C) approached the T_g of PET, variant Bhr-NMT showed markedly enhanced degradation activity, achieving conversions of 67.9%, 68.8%, and 72.7% within 8 h, equivalent to 1.22, 1.09, and 1.10 times higher than LCC-ICCG, respectively. In the temperature range of 68°C - 75°C , Bhr-NMT activity progressively increased with temperature, suggesting that it possesses adequate thermal stability to maintain the structural integrity of its active site even at 75°C . The conversion of Bhr-NMT sharply decreased to 28.2% as the temperature rose to 80°C , corresponding with an increase in enthalpy in its temperature-enthalpy curve (Fig. S15) that suggests the onset of secondary structure loss. At the optimal reaction temperature of 68°C for PET depolymerization, a series of evaluations of variant Bhr-NMT were conducted in the pH range of 6.0–10.0 (Fig. S5). The optimum pH of Bhr-NMT

Fig. 3 | Computational loop reconstruction guided redesign of PET hydrolase Bhr-PETase and experimental characterization of the designed variants. **a** Fifty de novo designed loop structures. The structures of the β 6- β 7 loop (L187-T195) were remodeled using Modeler and are shown in cartoon models in different colors. **b** Structure of Loop10. The Van der Waals repulsion between two atoms is shown in dashed lines colored in red. The distance between two atoms, which is greater than the sum of their Van der Waals radii, is represented by a dashed line colored in blue. In loop remodeled structure (Loop10), the closest distances from the side chain and backbone of residue W190 to PET model substrate are 4.2 Å ((W190) CG-C18 (PET)) and 2.8 Å ((W190) CB-C18 (PET)), respectively. In the structure of Loop10, residues within the β 6- β 7 loop region clash with each other. The closest distance between residues F222 and H191 is 1.7 Å ((H191) CB-CZ (F222)), and the closest distance between residues H218 and W190 is 2.3 Å ((W190) NE1-NE2 (H218)). **c, d** Catalytic indicators were calculated from the high-throughput MD simulations (10×1 ns) for the designed variants. The orange squares represent the double variants (M1 + single mutation), while the green squares indicate the triple variants (M1 + double mutations). **e** Computed binding geometries of double variant M10(F222M/F243T) based on the structure of Loop10. The closest distance between residues M222 and H191 is 3.2 Å ((H191) CB-CE (M222)), and the closest distance between residues H218 and W190 is 2.3 Å ((W190) NE1-NE2 (H218)). **f** Computed binding geometries of triple variant M20(H218N/F222M/F243T) based on the structure of Loop10. The closest distance between residues M222 and H191 is 3.3 Å ((H191) CB-CE (M222)), and the closest distance between residues N218 and W190 is 3.0 Å ((W190) NE1-OD1 (N218)). Residue N218 forms a hydrogen bond with P214 (P214) O-ND2 (N218): 3.1 Å. **g, h** Catalytic activity and thermal stability evaluation of the designed variants. **g** Double variants (M1 + single mutation). **h** Triple variants (M1 + double mutations).



was 8.0, consistent with that of most PET hydrolases^{19,27,31,42,43}. As the pH increased, the proportion of TPA in the products rose, probably due to MHET hydrolysis in the buffer under alkaline conditions. A time-course activity comparison of Bhr-NMT and LCC-ICCG was conducted using 0.16% (w/v) P_c-PET concentration at 68 °C for 8 h (Fig. 4b). The conversion of Bhr-NMT at 4 h, 8 h, and 12 h was 49.5%, 71.7%, and 90.7%, respectively, representing 1.24, 1.12, and 1.17 times higher than those of LCC-ICCG. For

amorphous Gf-PET films (Goodfellow, Ø6 mm), Bhr-NMT also exhibited a faster degradation rate than LCC-ICCG, achieving 1.58 and 1.24 times higher conversion at 12 and 24 h, respectively (Fig. S11). Although Bhr-NMT exhibited the fastest catalytic depolymerization rate at 75 °C under low PET concentration, studies have indicated that PET crystallinity increases rapidly at 75 °C²⁷, limiting the overall PET conversion under industrially relevant conditions.

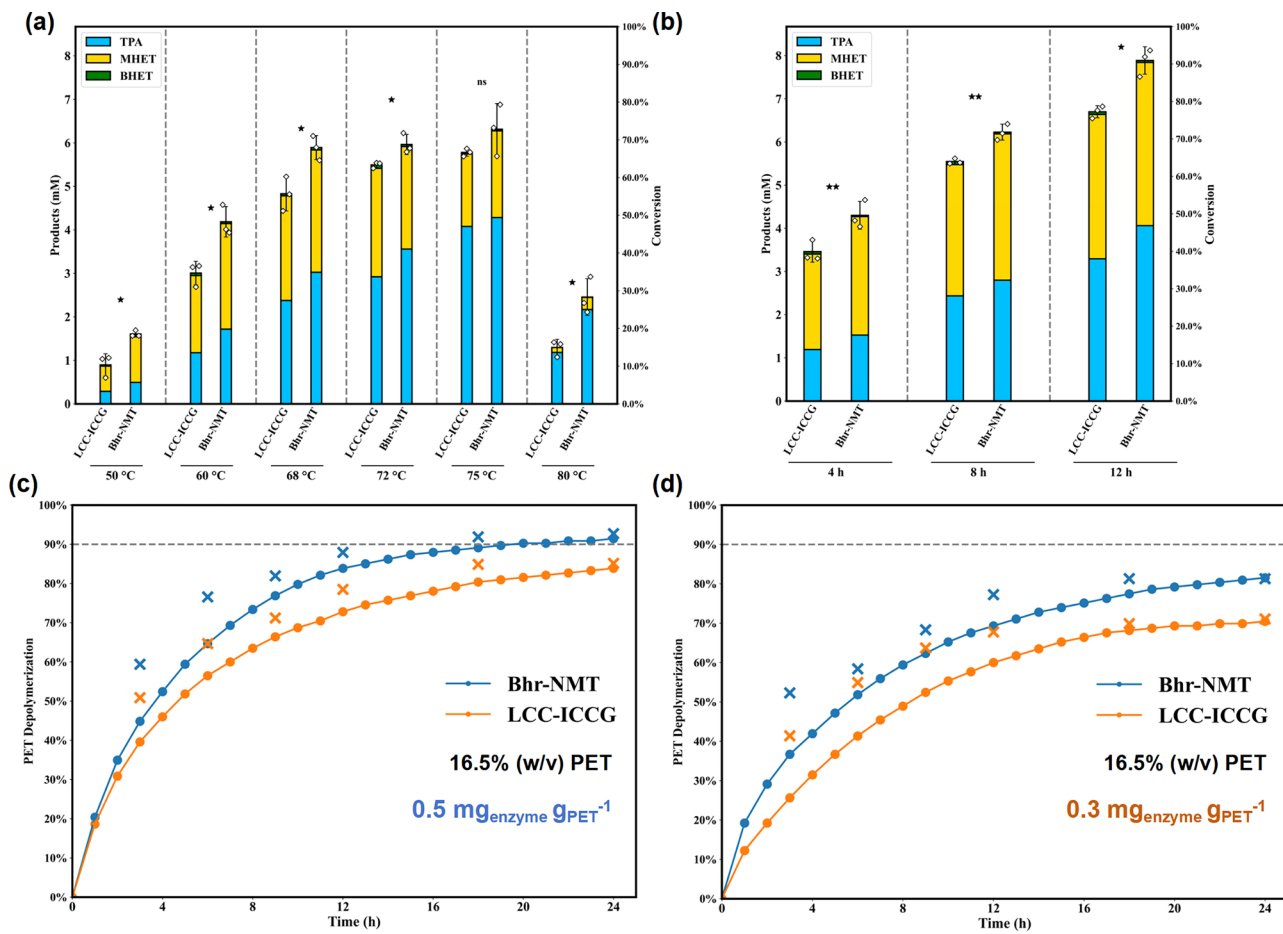


Fig. 4 | Experimental characterization of the highly active variant Bhr-NMT under industrial conditions. a Comparison of PET depolymerization by Bhr-NMT and LCC-IICG over a temperature range of 50 °C–80 °C. Reactions were conducted in triplicate, using 0.16% (w/w) amorphized Pc-PET powder and 1 mg_{enzyme} g_{PET}⁻¹ in 100 mM phosphate buffer (pH 8.0) for 8 h. **b** Time-course analysis of PET depolymerization by Bhr-NMT and LCC-IICG at 68 °C over 12 h. Reactions were conducted in triplicate, using 0.16% (w/w) of amorphized Pc-PET powder and 1 mg_{enzyme} g_{PET}⁻¹ in 100 mM phosphate buffer (pH 8.0). Unpaired, one-tailed *t*-tests were implemented to statistically assess differences in enzymatic product yields between different PET hydrolases (“*”: $P < 0.05$, “**”: $P < 0.01$, “***”: $P < 0.001$,

“ns”: the group not statistically significant ($P \geq 0.05$); exact *P* values are provided in the Supplementary Data File 1). The error bars represent the standard deviation of all products for each enzyme. **c, d** Comparison of PET depolymerization by Bhr-NMT and LCC-IICG under high PET substrate concentrations in a bioreactor. The reaction system had a total volume of 50 ml, containing 16.5% (w/v) amorphized Pc-PET powder and 0.5 mg_{enzyme} g_{PET}⁻¹ (or 0.3 mg_{enzyme} g_{PET}⁻¹) in 100 mM phosphate buffer at pH 8.0. The circles represent the conversion measured by the consumption of NaOH, while the crosses indicate the conversion calculated by HPLC analyses. The detailed data were provided in Table S10.

To further investigate the effectiveness of enzymes in catalyzing PET depolymerization under industrial conditions, Bhr-NMT and LCC-IICG were evaluated using amorphized PET powder (7.33% crystallinity) in a bioreactor under high PET concentrations. To ensure accurate measurement of hydrolysis products, the reaction conditions were set as follows: a substrate concentration of 165 g kg⁻¹ (representing the maximum solubility of terephthalate at 70 °C³³) and an enzyme loading of 0.5 mg_{enzyme} g_{PET}⁻¹. The reaction was conducted in a 100 mM phosphate buffer at 70 °C for 24 h, with the pH value maintained at 8.0 by the addition of 5 M NaOH solution. The conversion of PET was determined from the volume of NaOH solution added (Fig. 4c) and the HPLC analysis results of the products at various times (Table S10). Bhr-NMT achieved 59% (3 h) and 92% (18 h) PET conversion, corresponding to 1.16 and 1.08 times enhancements relative to LCC-IICG. Over 24 h, Bhr-NMT converted 93% of PET into TPA, MHET, and EG, whereas LCC-IICG achieved 85% overall conversion. Under conditions of reduced enzyme loading (165 g kg⁻¹ substrate concentration and 0.3 mg_{enzyme} g_{PET}⁻¹ enzyme loading), Bhr-NMT demonstrated a wider performance margin compared to the benchmark LCC-IICG, achieving 81% overall conversion in 24 h, whereas LCC-IICG only reached 71% (Fig. 4d and Table S11).

Transplant of loop reconstruction mutations to other PET hydrolases

Considering the high homology of PET hydrolases, it was hypothesized that the β6-β7 loop in other PET hydrolases may cause structural clashes with PET. Transferring mutations that alter the loop structure (H218N/F222M) to other PET hydrolases may enhance their catalytic activity. Therefore, two engineered enzymes were selected as templates: (i) LCC-IICG²⁷, a variant of thermostable cutinase LCC, and (ii) Kubu-P^{M12}⁴⁵, a variant of Kubu-P derived from *Kutzneria buriramensis* DSM 45791. By introducing the H218N/F222M mutations into these enzymes, we successfully constructed the recombinant proteins LCC-IICG-NM and Kubu-P^{M12}-NM.

LCC-IICG and Bhr-PETase share 92.6% sequence identity (Fig. S16), which confers high structural similarity between these two enzymes. The crystal structures of the two enzymes were aligned (Fig. 5a), revealing a backbone RMSD of 0.678 Å, along with an RMSD of 0.523 Å for the catalytically relevant residues (catalytic triad and oxyanion hole residues). Despite a low sequence identity (42.9%, Fig. S17) between Kubu-P^{M12} and Bhr-PETase, structural analysis revealed their shared α/β hydrolase fold with six α-helices and nine antiparallel β-strands. Structural alignment of the two enzymes revealed an RMSD of 0.574 Å for catalytic residues and 0.977 Å for backbone atoms in the β6-β7 loop (Fig. 5b).

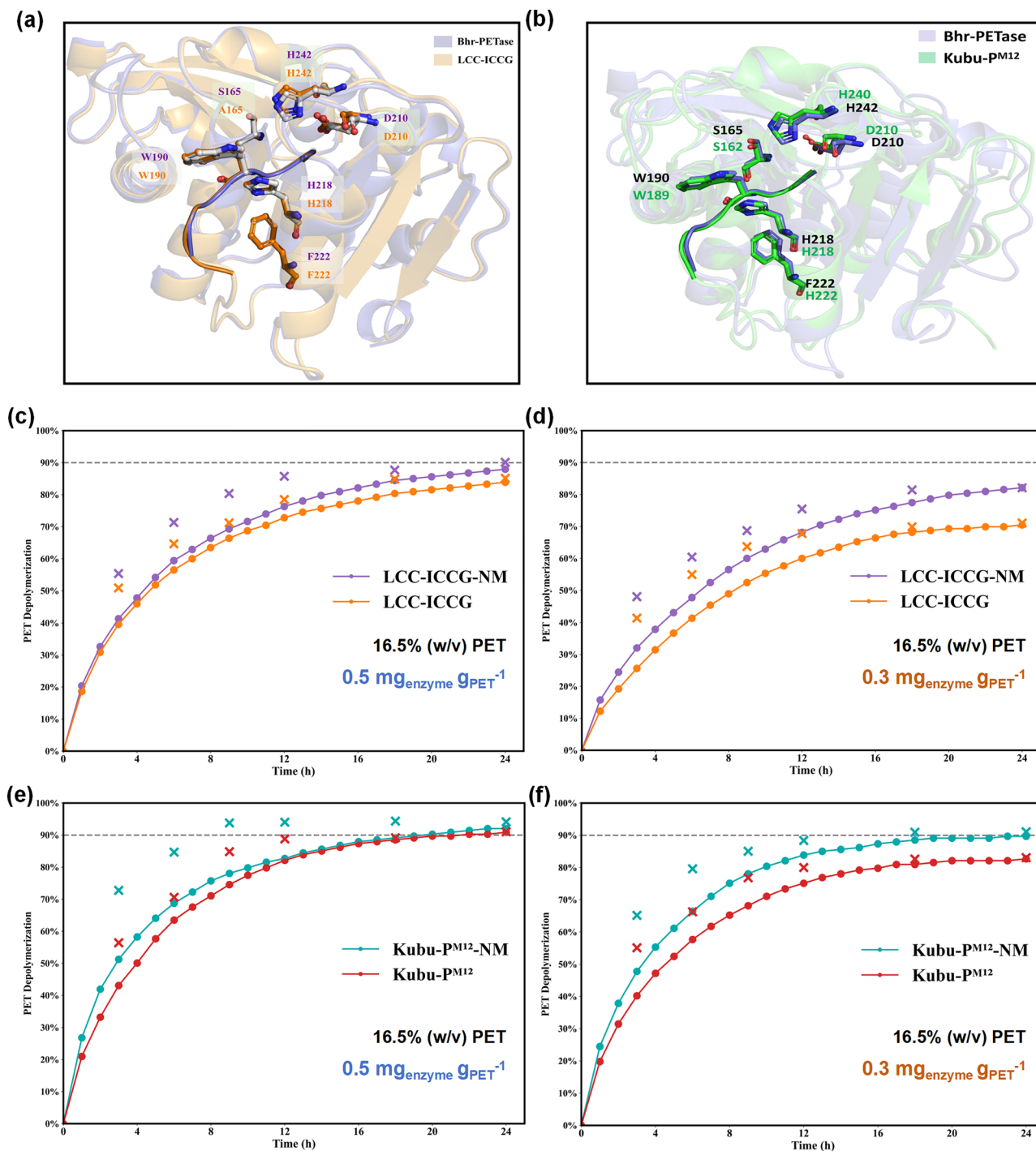


Fig. 5 | Transplant of loop reconstruction mutations to create the highly active PET hydrolases LCC-ICCG-NM and Kubu-P^{M12}-NM, and their experimental characterization under industrial conditions. **a**, Structure alignment between Bhr-PETase (PDB ID:7EOA, colored in purple) and LCC-ICCG (PDB ID:6THT, colored in orange). The catalytic residue serine (S165) was mutated to alanine in the crystal structure of LCC-ICCG. **b**, Structure alignment between Bhr-PETase (PDB ID:7EOA, colored in purple) and Kubu-P^{M12} (PDB ID:8YTY, colored in green). **c, d**, Comparison of PET depolymerization by LCC-ICCG-NM and LCC-ICCG under high PET substrate concentrations in a bioreactor. The reaction system had a

total volume of 50 ml, containing 16.5% (w/v) amorphized Pc-PET powder and 0.5 mg_{enzyme} g_{PET}⁻¹ (or 0.3 mg_{enzyme} g_{PET}⁻¹) in 100 mM phosphate buffer at pH 8.0. **e, f**, Comparison of PET depolymerization by Kubu-P^{M12}-NM and Kubu-P^{M12} under high PET substrate concentrations in a bioreactor. The reaction system had a total volume of 50 ml, containing 16.5% (w/v) amorphized Pc-PET powder and 0.5 mg_{enzyme} g_{PET}⁻¹ (or 0.3 mg_{enzyme} g_{PET}⁻¹) in 100 mM phosphate buffer at pH 8.0. The circles represent the conversion measured by the consumption of NaOH, while the crosses indicate the conversion calculated by HPLC analyses.

The H218N/F222M double mutations maximally preserve the enzyme's thermal stability. The protein melting curves (Fig. S15) demonstrated that the designed variants LCC-ICCG-NM ($T_m = 92.4^\circ\text{C}$) and Kubu-P^{M12}-NM ($T_m = 92.9^\circ\text{C}$) retained comparable stability to their respective templates LCC-ICCG ($T_m = 94.6^\circ\text{C}$) and Kubu-P^{M12}

($T_m = 97.4^\circ\text{C}$), enabling sustained catalytic activity under prolonged industrial depolymerization conditions ($68\text{--}70^\circ\text{C}$). The pH-dependent experiments (Figs. S5 and S6) revealed that both variants LCC-ICCG-NM and Kubu-P^{M12}-NM exhibited optimal activity at pH 8.0, which was consistent with their respective templates. Within the temperature range of

50 °C–75 °C, both variants exhibited higher catalytic activity compared to their respective templates (Figs. S7 and S8). The PET conversions of the variants increased progressively with rising temperature, indicating that their binding pockets maintained structural integrity even at 75 °C. Time-course PET depolymerization assays revealed that the designed variants significantly enhanced the hydrolysis efficiency of PET. After 4 h and 12 h, LCC-ICCG-NM achieved 48% and 91% conversion (1.22 and 1.18 times higher than LCC-ICCG, Figs. S9), while Kubu-P^{M12}-NM reached 50% and 91% (1.55 and 1.07 times higher than Kubu-P^{M12}, Figs. S10 and S12).

To assess the performance of LCC-ICCG-NM and Kubu-P^{M12}-NM in catalyzing PET depolymerization under industrial conditions, evaluations were conducted under high PET concentrations (temperature: 70 °C, 165 g kg⁻¹ of PET concentration, with an enzyme loading of 0.5 mg_{enzyme} g_{PET}⁻¹). Both LCC-ICCG-NM and Kubu-P^{M12}-NM showed superior PET depolymerization performance compared to their respective templates. Kubu-P^{M12}-NM exhibited the highest catalytic efficiency among all PET hydrolases, reaching 73% conversion within 3 h (1.29 times higher than Kubu-P^{M12}), surpassing 90% conversion by 9 h, and achieving 94% overall conversion after 24 h (Fig. 5e). The variant LCC-ICCG-NM showed improved catalytic performance with 90% overall conversion (Fig. 5c), outperforming the template LCC-ICCG (85%). The performance advantage of the engineered variants over their respective templates was further enhanced under reduced enzyme loading (0.3 mg_{enzyme} g_{PET}⁻¹). Kubu-P^{M12}-NM still showed the highest degree of the PET depolymerization, reaching 65% conversion in 3 h and exceeding 90% conversion after 18 h. The overall conversion of Kubu-P^{M12}-NM, Kubu-P^{M12}, LCC-ICCG-NM and LCC-ICCG was 91%, 83%, 82% and 71%, respectively (Fig. 5e, f).

To further investigate the effect of the H218N/F222M double mutations on PET degradation, the molecular weight of the PET substrate was measured throughout the reaction process catalyzed by Kubu-P^{M12}-NM. The initial molecular weight of the PET substrate was 52.7 kDa, which decreased to 36.3 kDa after 6 h and further declined to 31.5 kDa after 24 h. The reconstruction of the β6-β7 loop aims to modify the backbone structure of the PET hydrolase to enhance its compatibility with the dominant conformation of PET chains. In the initial phase, the high molecular weight of the PET substrate maintains the structural characteristics of the amorphous polymer (the torsional angle of the ethylenic bond (O-C-C-O) is ~−70°), while the rapid decrease in molecular weight indicates that Kubu-P^{M12}-NM primarily catalyzes the cleavage of inter-chain ester bonds (endo-type degradation). The significant enhancement in catalytic efficiency further validates the effectiveness of our design strategy. As PET depolymerized and the molecular weight of the substrate continuously decreased, it was hypothesized that the torsion angle of the ethylenic bond would further extend toward −180°. The change in the torsional angle reduces the structural compatibility between the substrate and Kubu-P^{M12}-NM, leading to a decline in its depolymerization activity. The structural mismatch also resulted in the designed variants achieving an overall conversion of no more than 40% for semicrystalline PET (Figs. S13 and S14).

It is noteworthy that the introduction of double mutations (H218N/F222M) in LCC-ICCG significantly enhances the expression levels of the target protein in *E. coli*. The variant LCC-ICCG-NM achieved a protein yield of 92 mg l⁻¹ during shake flask cultivation, which was 3.3 times higher than LCC-ICCG (Fig. S20). A fed-batch fermentation was conducted for 38 h in a 5 L bioreactor to produce LCC-ICCG-NM in recombinant *E. coli* containing the target protein gene, resulting in a protein yield of 1.49 g l⁻¹ (Fig. S20). The method of heating fermentation products at 60 °C has been demonstrated to yield pure target proteins effectively, and this simple purification method is well suitable for industrial applications. The activity of the enzymes obtained through this method was comparable to those purified through the Nickel-affinity chromatography column (Fig. S21), with 60.1% and 66.5% conversion in 8 h at 68 °C, respectively. Moreover, Kubu-P^{M12}-NM showed a 1.5 times increase in shake-flask protein yield compared to its template Kubu-P^{M12}, reaching 10 mg l⁻¹. The increased recombinant protein yield in the H218N/F222M variants was primarily due to enhanced solubility, as evidenced by a significant reduction in insoluble

aggregates in *E. coli* expressing LCC-ICCG-NM and Kubu-P^{M12}-NM compared to their respective templates (Fig. S19). Further genetic optimization of the expression system could potentially enhance the expression levels of the designed variants^{58,59}.

Structural insights of loop reconstruction mutations

The crystal structure of the highly active variant Bhr-NMT was measured and analyzed to verify whether the β6-β7 loop conformed to our computational design (Table S16). An alignment of the overall structures of the variant Bhr-NMT (PDB ID: 9KL9) and the wild-type Bhr-PETase (PDB ID: 7EOA) was shown in Fig. 6a. The RMSD of the atoms associated with the catalytic residues (catalytic triad and oxyanion hole) and the Ca atoms in the main-chain between the two proteins were 0.60 Å and 0.59 Å, respectively, indicating that the mutations did not significantly alter the residues at the catalytic site or the overall backbone structure of the protein. An alignment of Bhr-NMT and Bhr-PETase at the β6-β7 loop was shown in Fig. 6b, illustrating that the mutations caused a deviation in the position of the loop, with an RMSD of 0.82 Å (L187-K194). In Bhr-NMT, the residue W190 is positioned closer to the α5 helix compared to the wild-type, with a difference of 0.9 Å in the distance of the NE1 atom of W190 between the apo-form of the two enzymes. A repacking calculation based on the crystal structure of Bhr-NMT was performed, with the computed binding geometries shown in Fig. 6c. The backbone atom positions of residues N218 and M222 hardly deviated (Fig. 6b), while the minimum distances between PET and the side chain and backbone of W190 in Bhr-NMT increased by 0.5 Å and 0.2 Å, respectively, relative to the wild-type. The mutations shortened the distance between the β6-β7 loop and the α5 helix, shifting the loop away from the hydrolytic domain and expanding the enzyme's binding pocket to enhance PET polymer binding.

The crystal structures indicated that the hydrogen bonding network of the side chain at position 218 was altered by the mutation. In Bhr-NMT, residue N218 forms a hydrogen bond with residue P214 located in the β7-α5 loop, whereas in the wild type, residue H218 forms a hydrogen bond with residue H191 located in the β6-β7 loop. The hydrogen bonding interactions of residue 218 in both enzymes during MD simulations (Bhr-NMT: N218-P214: 63%, N218-H191: 13%; Wild-type: H218-P214: 8%, H218-H191: 84%. Table S12) were consistent with those observed in the crystal structure. Bhr-NMT possesses a larger binding pocket compared to the wild-type, which provides greater spatial freedom for the rotation of the β6-β7 loop, thereby facilitating improved binding affinity between the enzyme and PET. In Bhr-NMT, the hydrogen bond between residue N218 and P214 effectively links the α5 helix and the β7-α5 loop, playing a crucial role in maintaining thermal stability comparable to that of the wild-type. Guo et al. reported that residue W185, located in the β6-β7 loop of IsPETase, exhibits greater flexibility than the corresponding tryptophan residues in other homologous PET hydrolases, thereby enhancing its binding with PET³⁹. In the crystal structure of IsPETase (PDB ID: 5XJH, chain B³⁸), the side chain of residue S214 forms a hydrogen bond with P210 located in the β7-α5 loop (Fig. 6d). MD simulation analysis of IsPETase showed that the distance between residue S214 and the β6-β7 loop was greater than that to the β7-α5 loop, consistent with the trend observed in Bhr-NMT (Fig. S22).

The flexibility of residues associated with the β6-β7 loop structure in both the Bhr-NMT variant and the wild-type enzyme was examined through MD simulations (Fig. S23). In Bhr-NMT, the RMSD of residue W190 was slightly greater than that in the wild-type, consistent with the findings of Guo et al.³⁹. Additionally, compared to the relatively stable H218 and F222 residues in the wild-type, the RMSDs of residues N218 and M222 in Bhr-NMT showed an overall increase. In the MD simulations, the hydrogen bond linking the α5 helix and the β7-α5 loop (N218-P214) in Bhr-NMT was less stable than the hydrogen bond linking the α5 helix and the β6-β7 loop (H218-H191) in the wild-type, resulting in increased flexibility of N218. Methionine has more rotatable bonds than phenylalanine, facilitating a more favorable alignment of M222 with the flexible β6-β7 loop backbone during PET binding. Furthermore, M222 establishes stable hydrophobic

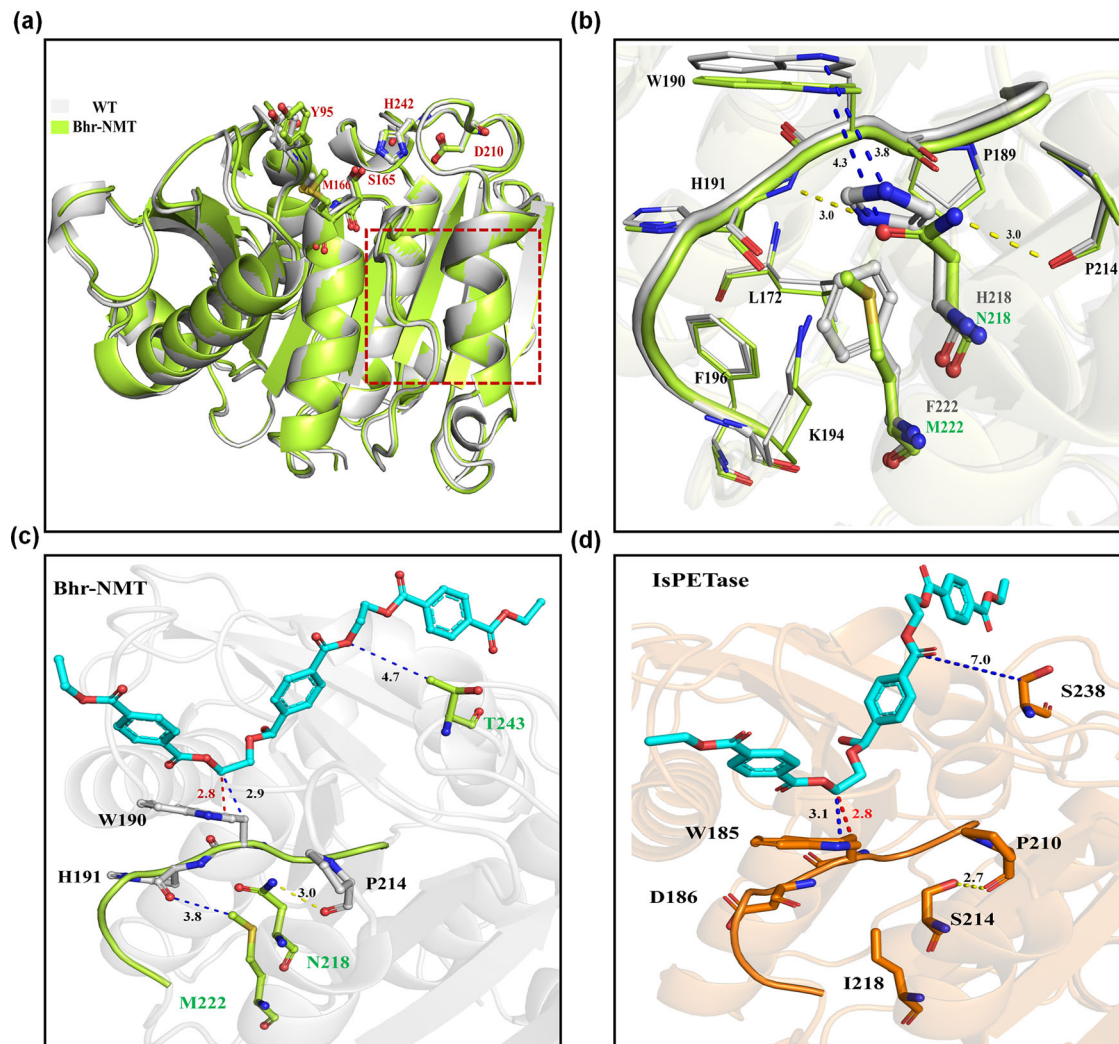


Fig. 6 | Structural insights of the highly active variant Bhr-NMT. **a** Structure alignment between the wild-type Bhr-PETase (PDB ID:7EOA, colored in gray) and the designed variant Bhr-NMT (PDB ID:9KL9, colored in lemon). The catalytic triad and the oxyanion hole residues are shown in the ball-and-stick model. The β₆-β₇ loop region is shown within the red dashed lines. **b** Structure alignment of the β₆-β₇ loops for the wild-type Bhr-PETase and the designed variant Bhr-NMT. The hydrogen bonds are shown in dashed lines colored in yellow. The dashed lines colored in blue indicate that the distance between these two atoms exceeds the sum of their Van der Waals radii. In the wild-type, the closest distance from the side chain of residue W190 to H218 is 3.8 Å ((W190) NE1-NE2 (H218)), and H191 forms a

hydrogen bond with H218 ((H191) NE1-N (H218): 3.0 Å). In Bhr-NMT, the closest distance between the side chains of residues W190 and N218 is 4.3 Å ((W190) NE1-OD1 (N218)), and P214 forms a hydrogen bond with N218 ((P214) O-ND2 (N218): 3.0 Å). **c** Computed binding geometries of variant Bhr-NMT based on the crystal structure (PDB ID: 9KL9). In Bhr-NMT, the closest distances of the side chain and backbone of residue W190 to PET are 2.8 Å ((W190) CG-C18 (PET)) and 2.9 Å ((W190) CB-C18 (PET)), respectively. **d** Computed binding geometries of PET hydrolase IsPETase based on its crystal structure (PDB ID:5XH3). In IsPETase, the closest distances of the side chain and backbone of residue W185 to PET are 3.1 Å ((W185) CG-C18 (PET)) and 2.8 Å ((W185) CB-C18 (PET)), respectively.

stacking with the surrounding hydrophobic residues L172 and F196, effectively maintaining the structural stability of the enzyme.

Discussion

Here, we developed a computational design approach based on the structural characteristics of PET polymers to modify the binding pocket of PET hydrolase Bhr-PETase. Through the remodeling and reconstruction of the β₆-β₇ loop, the variant Bhr-NMT (H218N/F222M/F243T) was successfully constructed, exhibiting an activity 1.87 times higher than that of the wild-type. Furthermore, the loop reconstruction mutations (H218N/F222M) were successfully transplanted into the well-known engineered PET hydrolases LCC-ICCG and Kubu-P^{M12}, resulting in the construction of the variants LCC-ICCG-NM and Kubu-P^{M12}-NM, which exhibit activities 1.22 and 1.55 times greater than their respective templates. Under large-scale reaction conditions (165 g kg⁻¹ substrate concentration and 0.5 mg_{enzyme} g_{PET}⁻¹ enzyme loading), the variants Kubu-P^{M12}-NM, Bhr-NMT, and LCC-ICCG-NM exhibited higher catalytic activity, achieving overall conversion

of 94%, 93%, and 90%, respectively, whereas the benchmark LCC-ICCG reached only 85%. It is noteworthy that when the enzyme loading was further reduced to 0.3 mg_{enzyme} g_{PET}⁻¹, the designed variants showed a more pronounced improvement in PET depolymerization efficiency compared to the benchmarks. Among all PET hydrolases, Kubu-P^{M12}-NM achieved the highest overall conversion of 91%, while LCC-ICCG and Kubu-P^{M12} reached only 71% and 83%, respectively.

Although multiple mutations at residues H218 or F222 in Bhr-PETase and LCC-ICCG have been previously reported^{19,31,60}, the double mutation H218N/F222M has not yet been found in either of these enzymes. Moreover, the double mutation H218N/F222M demonstrated the potential generalizability for boosting the performance of PET hydrolases. The double mutation was introduced into the LCC-ICCG (sequence identity: 92.6%) and Kubu-P^{M12} (sequence identity: 42.9%), resulting in designed variants, LCC-ICCG-NM and Kubu-P^{M12}-NM, which exhibited a significant enhancement in activity. PET hydrolases always share characteristic α/β-hydrolase domains and exhibit highly similar backbone conformations in

the β 6- β 7 loop. This structural convergence enabled the loop reconstructed design strategy based on Bhr-PETase to be successfully applied to other PET hydrolases, and the double mutation H218N/F222M will be introduced into more PET hydrolases to further verify its transplant generality.

While the remodeled loop structure generated with the classical protein modeling tool Modeler¹⁸ was successful to produce highly active PET hydrolases, the computational predictions still exhibit differences from those in the crystal structure. In future studies, more accurate loop structures may be generated by employing deep-learning based protein design tools, such as RFdiffusion⁶¹, ProteinMPNN⁶², and AlphaFold3⁶³. Our computational enzyme design strategy facilitates the screening and development of efficient PET hydrolases, advancing the industrialization of PET recycling.

Methods

Structural data

The PET model substrate was constructed using the Polymer Builder module of the molecular modeling tool CHARMM-GUI⁶⁴. Initially, four PET monomers (ethylene glycol terephthalate) were constructed using CHARMM-GUI, with both termini capped by hydrogen atoms. Subsequently, using the molecular editing software Pymol, one terminal 2-hydroxyethyl terephthalate group was removed to generate a compound comprising three PET monomers linked to an ethyl group, which was used as the model substrate for computational enzyme design and MD simulations in this study. The structure and atomic names for the model substrate are presented in Fig. S24. The crystal structures of the wild-type Bhr-PETase (PDB ID: 7EOA, the number of residue started from 36), IsPETase (PDB ID: 5XH3, the number of residue started from 30), LCC-ICCG (PDB ID: 6THT) and Kubu-PM12 (PDB ID: 8YTY) were obtained directly from the PDB database. The crystal structure of the variant Bhr-NMT was resolved and deposited into the PDB database (PDB ID: 9KL9). For the enzyme crystal structures used, water molecules and other small molecules were removed using PyMOL. Hydrogen atoms were added to all amino acids utilizing our in-house computational enzyme design tool PRODA^{47,48}, based on the topology parameters from the CHARMM 22 all-atom force field.

Computational enzyme design

The PET hydrolase Bhr-PETase was redesigned using our laboratory-developed computational enzyme design software PRODA^{47,48}. The workflow is presented in Fig. S25. For the specific design tasks, the sequence selection positions that allowed variation of the amino acid type and the residues that provided optimal side-chain conformations are shown in Table S13. A backbone-independent rotamer library comprising 11,810 original rotamers was used to model the side-chain conformations of the designed positions. In addition, the crystal conformations in the design positions of the template were included in the rotamer library. The rotamers for serine, threonine, and tyrosine were expanded due to adopting different conformations for the hydroxyl hydrogen atoms. The structure of the PET model substrate in the transition state (TS) was modified by altering the central ester bond's atom to achieve a tetrahedral geometry, with the specific internal coordinate for atoms obtained from the multiscale QM/MM MD simulations by Moliner et al.⁴⁹. The atomic van der Waals parameters of the PET model substrate were derived from the model molecules of the CHARMM 22 force field, and the charges for atoms were obtained from the CGENFF website. The TS conformational library was generated and screened based on the substrate placement rules (Table S1) and the catalytic geometric constraints (Table S2), utilizing the small-molecule placement approach in PRODA^{47,48}. The free energy of the enzyme-substrate complex in the TS was calculated by the energy functions in PRODA, and the sequences were optimized by the deterministic global optimization algorithm.

Molecular dynamics simulation

All MD simulations were conducted using GROMACS version 2022.5⁶⁵. The initial complex coordinates of designs were derived from the computational results of PRODA. The enzyme-PET complex structure was

embedded within a dodecahedral box whose size was determined by setting the distance between the solute and the box to 10 Å. Approximately 8500 display water molecules were added within the box, with the water model selected being TIP3P under the CHARMM36 force field⁶⁶. The charge of the system was neutralized by adding an appropriate number of Na⁺ or Cl⁻ counter ions to the solvent box.

Each simulation was independently initiated with energy minimization (EM) of the system using the steepest descent minimization algorithm. The EM continued until the potential energy was negative, and the maximum force Fmax did not exceed 1000 kJ mol⁻¹ nm⁻¹. Next, the system was subjected to position-restrained NVT simulations using the simulated annealing method. For the 1 ns and 5 ns MD simulations, the temperature was gradually increased from 0 to 343 K throughout 200 ps. Subsequently, the system underwent 200 ps of position-restrained NPT simulations. The time step for both NVT and NPT was set to 2 fs. The velocity rescaling thermostat was used for temperature control, and the Berendsen barostat was employed for pressure control. The LINCS algorithm was used to impose constraints on bonds and angles of the complex, and the Particle-Mesh-Ewald method was used to model long-range electrostatic effects, and short-range Van der Waals interactions were cut off at 12 Å, and the differential equations of motion were integrated by a leap-frog algorithm. The 1 ns and 5 ns MD simulations were performed 10 and 5 times, respectively; the time step was set to 2 fs for both; coordinates of all atoms in the system were saved every 1 ps and 5 ps, respectively, with a total of 1000 frames generated for each. Data generated from the MD simulations were extracted and analyzed using the Python package Mdanalysis, while the interactions between the enzyme and substrate were analyzed and visualized with PyMOL software. More details are presented in the supporting information (Table S14).

Loop remodeling

The β 6- β 7 loop in the wild-type Bhr-PETase crystal structure (PDB ID: 7EOA) was remodeled using the protein modeling tool Modeler 10.5¹⁸. First, water molecules and other small ligands were removed from the crystal structure by PyMOL, and the Bhr-PETase sequence was extracted from the PDB file. Next, residues L187 to T195 (L187, T188, P189, W190, H191, T192, D193, K194, T195) in Bhr-PETase were designated for remodeling, resulting in the generation of 50 distinct conformations. These conformations were then evaluated using the DOPE scoring method¹⁸.

Sequence alignment

A global sequence alignment between PET hydrolases LCC-ICCG and Bhr-PETase was conducted using the Needle tool from the EMBL-EBI bioinformatics platform (https://www.ebi.ac.uk/jDispatcher/psa/emboss_needle), yielding a pairwise alignment and calculating sequence similarity between the two enzymes. The alignment results were then visualized using the sequence alignment visualization tool ESPript 3.0 (<https://escript.ibcp.fr/EScript/EScript/>), as shown in Figs. S16 and S17.

Chemicals

Bis(2-hydroxyethyl) terephthalate (BHET) and mono(hydroxyethyl) terephthalate (MHET) were obtained from Bide Pharmatech Ltd (Shanghai, China). Terephthalic acid (TPA) was sourced from Maiklin Biochemical Technology Ltd (Shanghai, China).

Gene cloning, plasmid construction, and site-directed mutagenesis

The amino acid sequence of Bhr-PETase was obtained from the NCBI database (<https://www.ncbi.nlm.nih.gov/>), Bhr-PETase Genebank code: GBD22443.1). The amino acid sequences of LCC-ICCG and Kubu-PM12 were sourced from Tournier et al.²⁷ and Seo et al.⁴⁵. Codon optimization and gene synthesis were conducted by the Beijing Genomics Institution (Beijing, China). All nucleotide sequences were subcloned between the NdeI and XhoI restriction enzyme sites of the pET-22b(+) bacterial expression plasmid, fusing a 6 × hexahistidine tag-coding sequence to the C-terminus

of the enzyme. The variants of Bhr-PETase, LCC-ICCG, and Kubu-P^{M12} were generated through site-directed mutagenesis and verified using automated DNA sequencing technology. The amino acid sequences of Bhr-PETase, Bhr-NMT, LCC-ICCG, LCC-ICCG-NM, Kubu-P^{M12}, and Kubu-P^{M12}-NM were presented in Table S17.

Enzyme expression and purification

The plasmids containing the genes for the PET hydrolases BhrPETase, LCC-ICCG, Kubu-P^{M12}, and their mutants were transformed into *E. coli* strain BL21 (DE3), and the strains were cultured on solid Luria-Bertani (LB) medium with 100 µg ml⁻¹ ampicillin at 37 °C for 14–18 h. A well-grown single colony was transferred to 5 ml of LB liquid medium containing 100 µg ml⁻¹ ampicillin to prepare a seed solution, which was then incubated at 37 °C and 200 rpm for 7 h until the OD₆₀₀ value reached a 1.6–2.0. Then, 2 ml of the seed solution was transferred to 200 ml of LB liquid medium containing 100 µg ml⁻¹ ampicillin and incubated under conditions of 37 °C and 200 rpm until the OD₆₀₀ reached 0.6–0.8. For LCC-ICCG, Kubu-P^{M12}, and their variants, a final concentration of 0.5 mM IPTG was added to the shake flasks and incubated at 20 °C and 180 rpm for 16.5 h. For Bhr-PETase and its variants, 0.2% (w/v) L-arabinose was added to the culture and incubated at 20 °C and 180 rpm for 14.5 h. After centrifugation at 3819 × g for 20 min at 4 °C, all cell pellets were resuspended in lysis buffer (100 mM phosphate, 300 mM NaCl, pH 8.0) and then subjected to a sonication cycle (4 s on and 6 s off) at 60% power for 45 min. The periplasmic extracts were centrifuged at 4 °C and 5198 × g for 15 min, and the supernatant was then further centrifuged at 4 °C and 15292 × g for 10 min to remove insoluble cell debris. The clarified lysate was loaded into a 25 ml HisTrap HP column, and unbound proteins were washed out with the buffer (100 mM phosphate, 300 mM NaCl, 100 mM imidazole, pH 8.0), and the target proteins were eluted with an elution buffer (100 mM phosphate, 300 mM NaCl, 400 mM imidazole, pH 8.0). The target proteins were centrifuged at 3819 × g for 20 min at 4 °C triple times using a 10 kDa cut-off Amicon® Ultra 15 ml Centrifugal Filter device from EMD Millipore Corporation (Billerica, USA) to desalte. The purified protein was stored at 4 °C, and its concentration was measured using Coomassie Brilliant Blue G250 from Solarbio (Beijing, China) and a UV-1200 spectrophotometer from Macylab Instrument Ltd (Shanghai, China). The presence and purity of the target protein were detected using sodium dodecyl sulfate-polyacrylamide gel electrophoresis (SDS-PAGE) (Figs. S18 and S19).

PET powder preparation

The microcrystalline post-consumer PET (Pc-PET, 10.61% crystallinity) for evaluating the activity of the variants was obtained from commercial bottles (body only; the neck and base were removed from the bottle) from the Coca-Cola Company (China). PET bottles were cut into 10 × 10 mm pieces and washed sequentially with water, 0.5% sodium dodecyl sulfate (SDS), and ethanol. After drying, the PET pieces were shredded into particles using an AM500S high-speed rotary mill from Ants Scientific Instruments Ltd (Beijing, China) equipped with a 0.5 mm trapezoidal hole sieve ring. During operation, the machine generated substantial heat, causing internal temperatures to exceed 200 °C. Upon opening, the PET powders were rapidly cooled to ambient temperature (~25 °C), effectively lowering their crystallinity. The powders were sifted through 200, 355 µm sieves, to obtain PET powders with particle sizes of 200–355 µm.

The amorphized Pc-PET (7.33% crystallinity) for PET depolymerization bioreactor assay was obtained from commercial bottles from the Coca-Cola Company (China). The PET bottles were initially washed with water, followed by heating in a muffle furnace at 290 °C for 15 min until complete melting. After heating, the melted PET was rapidly cooled in an ice-water bath to solidify. After drying, the PET pieces were shredded into particles using CM101 high-speed cutting mill from Grinder Instruments Ltd (Beijing, China), equipped with a 0.5 mm trapezoidal hole sieve ring. The powders were sifted through 200, 355 µm sieves to obtain PET powders with particle sizes of 200–355 µm.

PET depolymerization assay

PET depolymerization experiments with 0.16% (w/v) PET concentration were conducted to evaluate the activity of the Bhr-PETase variants. 5 mg of microcrystalline Pc-PET powder was soaked in 3 ml of 100 mM phosphate buffer (pH 8.0), with 0.057 µM of purified enzyme (1 mg_{enzyme} g_{PET}⁻¹) at 68 °C for 12 h. Equal volumes of methanol were added to terminate the reaction, and the supernatant was collected by centrifugation (10610 × g, 3 min). Each sample was diluted 10-fold and filtered through a 0.22 µm Millex filter. The contents of PET hydrolysis products (BHET, MHET, and TPA) were quantitatively analyzed using HPLC (Fig. S26). Each independent experiment was conducted in triplicate, with mean values and standard deviations subsequently calculated.

PET depolymerization bioreactor assay

PET depolymerization experiments in a bioreactor with a 16.5% (w/v) PET concentration were conducted to assess the catalytic activities of the PET hydrolases Bhr-NMT, LCC-ICCG, LCC-ICCG-NM, Kubu-P^{M12}, and Kubu-P^{M12}-NM at substrate concentrations relevant to industrial scale. 8.25 g of amorphized Pc-PET powders (corresponding to the volume of 6 ml, with PET density of 1.37 g ml⁻¹) were soaked into 44 ml of 100 mM phosphate buffer (pH 8.0) in a three-necked flask. The total system volume was 50 ml, with an enzyme concentration of 2.23 µM (0.5 mg_{enzyme} g_{PET}⁻¹) or 1.34 µM (0.3 mg_{enzyme} g_{PET}⁻¹). The three-necked flask was placed in a heat-collecting constant temperature magnetic stirrer ZNCL-G from YUHUA Instrument Ltd (Henan, China) to agitate the reaction solution and maintain the temperature at 70 °C. The pH of the reaction solution was continuously measured using a pH meter FE28 from Mettler Toledo (Zurich, Switzerland). A 5 M NaOH solution was added to adjust the pH to a range of 7.8–8.2, with the volume of NaOH solution added recorded. At 3, 6, 9, 12, 18, and 24 h, 1000 µl samples were extracted and combined with an equal volume of methanol to terminate the reaction. The samples were diluted to a suitable concentration, centrifuged, and filtered through a 0.22 µm Millex filter. The concentrations of BHET, MHET, and TPA in the diluted samples were quantitatively determined using HPLC. After the reaction, the residual PET substrate was washed with water, filtered through a 0.22 µm membrane, and dried at 50 °C for 48 h for weighing.

HPLC method

The concentrations of TPA, MHET, and BHET were determined using the CMB-20A system from Shimadzu Ltd (Kyoto, Japan) connected to an SPD-20A UV/Vis detector and a SunFire™ C18 column (5 µm, 4.6 × 250 mm) at 254 nm, with quantitative analysis performed using a calibration curve (Fig. S26). A volume of 10 µL from each sample was injected, and TPA, MHET, and BHET were separated using an eluent composed of acetonitrile and 0.1% (v/v) formic acid in water. The acetonitrile concentration was maintained at 5% for the first 5 min, then increased to 44% at 13 min, and further raised to 70% at 18 min, remaining at 70% until 23 min.

Determination method for protein melting temperature

The protein melting temperature (T_m) of each enzyme was determined using nano differential scanning fluorimetry (nanoDSF) with the protein stability analyzer Prometheus Panta from NanoTemper (Munich, Germany). During the measurement, the samples were heated from 25 °C to 110 °C at a rate of 2 °C min⁻¹. The T_m value of each enzyme was analyzed in triplicate, with mean values and standard deviations calculated accordingly.

Determination method for PET crystallinity

The crystallinity of microcrystalline Pc-PET, amorphized Pc-PET, amorphous Gf-PET (purchased from Goodfellow, product number ES301445), and semicrystalline PET were assessed using differential scanning calorimetry (DSC), as shown in Table S15. The sample (4–6 mg) was placed in an aluminum pan equipped with a solid sample lid. Next, the DSC 8000 system from PerkinElmer (Massachusetts, USA), with an automatic liquid nitrogen cooling system, was utilized to heat the sample from 30 °C to 300 °C at a rate of 10 °C min⁻¹, hold at 300 °C for 1 min, and subsequently cool back to

30 °C at the same rate. The crystallinity during the heating scan process was determined using the melting enthalpy (ΔH_m) and the cold crystallization enthalpy (ΔH_{cc}), according to the Eq. (1), where ΔH_m^0 refers to the melting enthalpy of 100% crystalline PET samples (140.1 J g⁻¹)⁶⁷.

$$\% \text{crystallinity} = \frac{[\Delta H_m - \Delta H_{cc}]}{\Delta H_m^0} \times 100\% \quad (1)$$

Determination method for molecular weight of PET

The molecular weight of the PET was analyzed using gel permeation chromatography (GPC) with an Agilent 1260 system from Agilent Technologies Ltd (California, USA) and a refractive index (RI) detector. The mobile phase consisted of 1, 1, 1, 3, 3, 3-hexafluoro-2-propanol (HFIP), and the analysis was conducted at 35 °C with a flow rate of 1 ml min⁻¹.

Fed-batch fermentation of *E. coli* strains

The fed-batch fermentation was applied to produce PET hydrolase LCC-ICCG-NM in recombinant *E. coli* BL21 (DE3) with a 5 L bioreactor. The strain was cultivated onto solid LB agar plates containing 100 µg ml⁻¹ antibiotics and incubated at 37 °C for 14 to 18 h. Well-grown individual colonies were then transferred to 5 ml of liquid LB medium containing 100 µg ml⁻¹ ampicillin and grown at 37 °C, 200 rpm for 12 h until the OD₆₀₀ reached 3.0–4.0. A 2 ml volume of the culture was inoculated into 50 ml of liquid LB medium to prepare a seed culture, which was grown at 37 °C and 200 rpm for 4 h until reaching an OD₆₀₀ of 1.5–2.5. The initial fermentation medium (2.0 L) was combined with 100 ml of seed culture (5% v/v) and transferred into a 5 l mechanically stirred fermenter BIOTECH-5JGZ from Baoxing Biological Equipment Engineering Ltd (Shanghai, China). The stirring speed was maintained between 300 and 600 rpm, with a gas flow rate of 0.3–0.6 vvm and pure oxygen enrichment at 0%–50%, ensuring dissolved oxygen levels remained above 5% of air saturation during fermentation. A two-stage temperature control was implemented, with the growth phase maintained at 37 °C for 0–14 h and 25 °C for protein production in the remainder of the fermentation. The pH was maintained at 7.0 by adding 5 M NH₄OH solution. The glucose content was monitored using the glucose meter ACCU-CHEK from Roche Diabetes Care GmbH Ltd (Basel, Switzerland). Protein expression was induced by adding Isopropyl β-D-1-thiogalactopyranoside (IPTG) at a final concentration of 1 mM over 14 h, with a total cultivation time of 38 h. After fermentation, the *E. coli* broth was centrifuged at 3819 × g for 30 min, and the pellet was resuspended in lysis buffer (100 mM phosphate, 300 mM NaCl, pH 8.0) and then subjected to a sonication cycle (4 s on and 6 s off) at 60% power for 45 min. The lysate was centrifuged at 5198 × g for 15 min at 4 °C to collect the supernatant. It was then centrifuged again at 15,292 × g for 10 min at 4 °C to remove insoluble cell debris, getting the crude enzyme solution containing the variant LCC-ICCG-NM. The crude enzyme solution was heated in a 60 °C water bath for 2 h to remove contaminating proteins, followed by centrifugation at 15292 × g for 30 min, obtaining the purified LCC-ICCG-NM in the supernatant. The presence and purity of the target protein were detected using SDS-PAGE.

Crystal structure determination

The designed PET hydrolase Bhr-NMT was concentrated to 4 mg ml⁻¹ in buffer containing 10 mM Tris-HCl (pH 8.0), 200 mM NaCl, and 5 mM dithiothreitol. Crystals were grown using the hanging-drop vapor diffusion method. Crystals of Bhr-PETase were grown at 18 °C by mixing an equal volume of the protein (4 mg ml⁻¹) with a reservoir solution containing 2.5 M Sodium chloride, 100 mM imidazole, and Hydrochloric acid (pH 8.0). The crystals appeared overnight and grew to a maximum size in ~2–3 days. The crystals were cryoprotected in a reservoir containing 20% glycerol before being transferred to liquid nitrogen. All data were collected at Shanghai Synchrotron Radiation Facility beamlines BL02U1, integrated, and scaled using the Aquarium⁶⁸. The initial model of Bhr-PETase was used

from PDB: 7EOA. The structure of Bhr-NMT was solved by molecular replacement and was refined manually using COOT⁶⁹. The structure was refined with PHENIX⁷⁰ using non-crystallographic symmetry and stereochemical information as constraints. The final structure was obtained through several rounds of refinement. The data collection and structure refinement statistics are summarized in Table S16. The accession number for the coordinate and structure factors reported in the present paper is PDB ID: 9KL9.

Statistics and reproducibility

PET hydrolysis assay activities at low PET substrate concentrations were obtained from the average of three parallel experiments. The feature values for the 1 ns and 5 ns MD simulations were averaged over 10 and 5 replications, respectively.

Reporting summary

Further information on research design is available in the Nature Portfolio Reporting Summary linked to this article.

Data availability

The data that support this study are available from the corresponding author (Y.Z.) upon request. The source data underlying Figs. 2–5 are provided as Supplementary Data File 1. The atomic coordinates and structure factors have been deposited in the Protein Data Bank (<https://www.wwpdb.org/>), with PDB ID code 9KL9. The design results of the experimental variants by PRODA and Modeler models for enzyme complexes are available at <https://github.com/yymyym2019/structures>.

Received: 8 May 2025; Accepted: 10 June 2025;

Published online: 17 June 2025

References

1. Plastics Recycling. S&P Global (2024). Available at: <https://www.spglobal.com/commodityinsights/en/ci/products/plastics-recycling-chemical-economics-handbook.html>.
2. Singh, A. et al. Techno-economic, life-cycle, and socioeconomic impact analysis of enzymatic recycling of poly (ethylene terephthalate). *Joule* **5**, 2479–2503 (2021).
3. Nisticò, R. Polyethylene terephthalate (PET) in the packaging industry. *Polym. Test.* **90**, 106707 (2020).
4. Kawai, F., Kawabata, T. & Oda, M. Current state and perspectives related to the polyethylene terephthalate hydrolases available for biorecycling. *ACS Sustain. Chem. Eng.* **8**, 8894–8908 (2020).
5. Tamargo, A. et al. PET microplastics affect human gut microbiota communities during simulated gastrointestinal digestion, first evidence of plausible polymer biodegradation during human digestion. *Sci. Rep.* **12**, 528 (2022).
6. Rahimi, A. & García, J. M. Chemical recycling of waste plastics for new materials production. *Nat. Rev. Chem.* **1**, 0046 (2017).
7. Paszun, D. & Spychaj, T. Chemical recycling of poly (ethylene terephthalate). *Ind. Eng. Chem. Res.* **36**, 1373–1383 (1997).
8. Zhou, L. et al. Alcoholysis of polyethylene terephthalate to produce diethyl terephthalate using choline chloride-based deep eutectic solvents as efficient catalysts. *Green. Chem.* **21**, 897–906 (2019).
9. Sinha, V., Patel, M. R. & Patel, J. V. PET waste management by chemical recycling: a review. *J. Polym. Environ.* **18**, 8–25 (2010).
10. Mican, J. et al. Exploring new galaxies: perspectives on the discovery of novel PET-degrading enzymes. *Appl. Catal. B Environ.* **342**, 123404 (2024).
11. Danso, D. et al. New Insights into the Function and Global Distribution of Polyethylene Terephthalate (PET)-Degrading Bacteria and Enzymes in Marine and Terrestrial Metagenomes. *Appl. Environ. Microbiol.* **84**, e02773–02717 (2018).
12. Wei, R. et al. Possibilities and limitations of biotechnological plastic degradation and recycling. *Nat. Catal.* **3**, 867–871 (2020).

13. Müller, R. J., Schrader, H., Profe, J., Dresler, K. & Deckwer, W. D. Enzymatic degradation of poly (ethylene terephthalate): rapid hydrolyse using a hydrolase from *T. fusca*. *Macromol. Rapid Commun.* **26**, 1400–1405 (2005).
14. Alves, N., Mano, J. F., Balaguer, E., Dueñas, J. M. & Ribelles, J. G. Glass transition and structural relaxation in semi-crystalline poly (ethylene terephthalate): a DSC study. *Polymer* **43**, 4111–4122 (2002).
15. Thomsen, T. B., Hunt, C. J. & Meyer, A. S. Influence of substrate crystallinity and glass transition temperature on enzymatic degradation of polyethylene terephthalate (PET). *New. Biotechnology* **69**, 28–35 (2022).
16. Boyd, S. U. & Boyd, R. H. Chain dynamics and relaxation in amorphous poly (ethylene terephthalate): a molecular dynamics simulation study. *Macromolecules* **34**, 7219–7229 (2001).
17. Wei, R. et al. Mechanism-based design of efficient PET hydrolases. *ACS Catal.* **12**, 3382–3396 (2022).
18. Webb, B. & Sali, A. Comparative protein structure modeling using MODELLER. *Curr. Protoc. Bioinform.* **54**, 5.6. 1–5.6. 37 (2016).
19. Pfaff, L. et al. Multiple substrate binding mode-guided engineering of a thermophilic PET hydrolase. *ACS Catal.* **12**, 9790–9800 (2022).
20. Stavila, E., Arsyi, R., Petrovic, D. & Loos, K. Fusarium solani pisi cutinase-catalyzed synthesis of polyamides. *Eur. Polym. J.* **49**, 834–842 (2013).
21. Senga, A. et al. Multiple structural states of Ca²⁺-regulated PET hydrolase, Cut190, and its correlation with activity and stability. *J. Biochem.* **169**, 207–213 (2021).
22. Wei, R. et al. Engineered bacterial polyester hydrolases efficiently degrade polyethylene terephthalate due to relieved product inhibition. *Biotechnol. Bioeng.* **113**, 1658–1665 (2016).
23. Shirke, A. N. et al. Stabilizing leaf and branch compost cutinase (LCC) with glycosylation: mechanism and effect on PET hydrolysis. *Biochemistry* **57**, 1190–1200 (2018).
24. Oda, M. et al. Enzymatic hydrolysis of PET: Functional roles of three Ca²⁺ ions bound to a cutinase-like enzyme, Cut190*, and its engineering for improved activity. *Appl. Microbiol. Biotechnol.* **102**, 10067–10077 (2018).
25. Then, J. et al. Ca²⁺ and Mg²⁺ binding site engineering increases the degradation of polyethylene terephthalate films by polyester hydrolases from *Thermobifida fusca*. *Biotechnol. J.* **10**, 592–Ca598 (2015).
26. Then, J. et al. A disulfide bridge in the calcium binding site of a polyester hydrolase increases its thermal stability and activity against polyethylene terephthalate. *FEBS Open Bio.* **6**, 425–432 (2016).
27. Tournier, V. et al. An engineered PET depolymerase to break down and recycle plastic bottles. *Nature* **580**, 216–219 (2020).
28. Chen, X.-Q. et al. Directional-path modification strategy enhances PET hydrolase catalysis of plastic degradation. *J. Hazard. Mater.* **433**, 128816 (2022).
29. Meng, S. et al. Deep learning guided enzyme engineering of *Thermobifida fusca* cutinase for increased PET depolymerization. *Chin. J. Catal.* **50**, 229–238 (2023).
30. Kato, S. et al. Long-term cultivation and metagenomics reveal ecophysiology of previously uncultivated thermophiles involved in biogeochemical nitrogen cycle. *Microbes Environ.* **33**, 107–110 (2018).
31. Cui, Y. et al. Computational redesign of a hydrolase for nearly complete PET depolymerization at industrially relevant high-solids loading. *Nat. Commun.* **15**, 1417 (2024).
32. Zheng, Y. et al. Dynamic docking-assisted engineering of hydrolases for efficient PET depolymerization. *ACS. Catalysis* **14**, 3627–3639 (2024).
33. Arnal, G. et al. Assessment of four engineered PET degrading enzymes considering large-scale industrial applications. *ACS Catal.* **13**, 13156–13166 (2023).
34. Han, X. & Pan, J. Polymer chain scission, oligomer production and diffusion: a two-scale model for degradation of bioresorbable polyesters. *Acta Biomater.* **7**, 538–547 (2011).
35. Williams, A. & Flory, P. J. Configurational statistics of poly (ethylene terephthalate) chains. *J. Polym. Sci. Part A-2 Polym. Phys.* **5**, 417–424 (1967).
36. Schmidt-Rohr, K., Hu, W. & Zumbulyadis, N. Elucidation of the chain conformation in a glassy polyester, PET, by two-dimensional NMR. *Science* **280**, 714–717 (1998).
37. Yoshida, S. et al. A bacterium that degrades and assimilates poly (ethylene terephthalate). *Science* **351**, 1196–1199 (2016).
38. Han, X. et al. Structural insight into catalytic mechanism of PET hydrolase. *Nat. Commun.* **8**, 2106 (2017).
39. Chen, C.-C. et al. General features to enhance enzymatic activity of poly (ethylene terephthalate) hydrolysis. *Nat. Catal.* **4**, 425–430 (2021).
40. Guo, B. et al. Conformational selection in biocatalytic plastic degradation by PETase. *ACS Catal.* **12**, 3397–3409 (2022).
41. Son, H. F. et al. Rational protein engineering of thermo-stable PETase from *Ideonella sakaiensis* for highly efficient PET degradation. *ACS Catal.* **9**, 3519–3526 (2019).
42. Cui, Y. et al. Computational redesign of a PETase for plastic biodegradation under ambient condition by the GRAPE strategy. *ACS Catal.* **11**, 1340–1350 (2021).
43. Lu, H. et al. Machine learning-aided engineering of hydrolases for PET depolymerization. *Nature* **604**, 662–667 (2022).
44. Bell, E. L. et al. Directed evolution of an efficient and thermostable PET depolymerase. *Nature. Nat. Catal.* **5**, 673–681 (2022).
45. Seo, H. et al. Landscape profiling of PET depolymerases using a natural sequence cluster framework. *Science* **387**, eadp5637 (2025).
46. Wei, R. et al. Biocatalytic degradation efficiency of postconsumer polyethylene terephthalate packaging determined by their polymer microstructures. *Adv. Sci.* **6**, 1900491 (2019).
47. Lei, Y., Luo, W. & Zhu, Y. A matching algorithm for catalytic residue site selection in computational enzyme design. *Protein Sci.* **20**, 1566–1575 (2011).
48. Huang, X., Han, K. & Zhu, Y. Systematic optimization model and algorithm for binding sequence selection in computational enzyme design. *Protein Sci.* **22**, 929–941 (2013).
49. Boneta, S., Arafet, K. & Moliner, V. QM/MM study of the enzymatic biodegradation mechanism of polyethylene terephthalate. *J. Chem. Inf. Model.* **61**, 3041–3051 (2021).
50. Vogel, K. et al. Enzymatic degradation of polyethylene terephthalate nanoplastics analyzed in real time by isothermal titration calorimetry. *Sci. Total Environ.* **773**, 145111 (2021).
51. He, J., Huang, X., Xue, J. & Zhu, Y. Computational redesign of penicillin acylase for cephradine synthesis with high kinetic selectivity. *Green. Chem.* **20**, 5484–5490 (2018).
52. Wang, P., Zhang, J., Zhang, S., Lu, D. & Zhu, Y. Using high-throughput molecular dynamics simulation to enhance the computational design of kemp elimination enzymes. *J. Chem. Inf. Model.* **63**, 1323–1337 (2023).
53. Zhang, S. et al. Computational redesign of an enoate reductase for the in vivo production of adipic acid from muconic acid. *Chem. Catal.* **4**, 2667–1107 (2024).
54. Hedenqvist, M., Bharadwaj, R. & Boyd, R. Molecular dynamics simulation of amorphous poly (ethylene terephthalate). *Macromolecules* **31**, 1556–1564 (1998).
55. Kuhlman, B. & Baker, D. Native protein sequences are close to optimal for their structures. *Proc. Natl. Acad. Sci. USA* **97**, 10383–10388 (2000).
56. Zhang, J. et al. Computational design of highly efficient thermostable MHET hydrolases and dual enzyme system for PET recycling. *Commun. Biol.* **6**, 1135 (2023).

57. Broom, A. et al. Ensemble-based enzyme design can recapitulate the effects of laboratory directed evolution in silico. *Nat. Commun.* **11**, 4808 (2020).
58. Soong, Y. H. V. et al. Enzyme selection, optimization, and production toward biodegradation of post-consumer poly (ethylene terephthalate) at scale. *Biotechnol. J.* **18**, 2300119 (2023).
59. Seman, W. W. et al. High level expression of *Glomerella cingulata* cutinase in dense cultures of *Pichia pastoris* grown under fed-batch conditions. *J. Biotechnol.* **184**, 219–228 (2014).
60. Orr, G. et al. Streamlined screening of extracellularly expressed PETase libraries for improved polyethylene terephthalate degradation. *Biotechnol. J.* **19**, 2400021 (2024).
61. Watson, J. L. et al. De novo design of protein structure and function with RFdiffusion. *Nature* **620**, 1089–1100 (2023).
62. Dauparas, J. et al. Robust deep learning-based protein sequence design using ProteinMPNN. *Science* **378**, 49–56 (2022).
63. Abramson, J. et al. Accurate structure prediction of biomolecular interactions with AlphaFold 3. *Nature*, **630**, 493–500 (2024).
64. Choi, Y. K. et al. CHARMM-GUI polymer builder for modeling and simulation of synthetic polymers. *J. Chem. Theory Comput.* **17**, 2431–2443 (2021).
65. Abraham, M. J. et al. GROMACS: High performance molecular simulations through multi-level parallelism from laptops to supercomputers. *SoftwareX* **1**, 19–25 (2015).
66. Yu, W., He, X., Vanommeslaeghe, K. & MacKerell, A. D. Jr Extension of the CHARMM general force field to sulfonyl-containing compounds and its utility in biomolecular simulations. *J. Comput. Chem.* **33**, 2451–2468 (2012).
67. Vertommen, M., Nierstrasz, V., Van Der Veer, M. & Warmoeskerken, M. Enzymatic surface modification of poly (ethylene terephthalate). *J. Biotechnol.* **120**, 376–386 (2005).
68. Yu, F. et al. Aquarium: an automatic data-processing and experiment information management system for biological macromolecular crystallography beamlines. *J. Appl. Crystallogr.* **52**, 472–477 (2019).
69. Emsley, P., Lohkamp, B., Scott, W. G. & Cowtan, K. Features and development of Coot. *Acta Crystallogr. Sect. D Biol. Crystallogr.* **66**, 486–501 (2010).
70. Adams, P. D. et al. PHENIX: building new software for automated crystallographic structure determination. *Acta Crystallogr. Sect. D Biol. Crystallogr.* **58**, 1948–1954 (2002).

Acknowledgements

We acknowledge the financial support from the National Key Research and Development Program of China (grant number:2021YFC2103600), the National Natural Science Foundation of China (grant number:21878170), the PetroChina (grant number: PRIKY23109), and the Fundamental Research Funds for the Central Universities (buctrc202136 and JD2103).

Author contributions

Y.Z. conceived the project. Hongzhao.W., Y.C., and Z.Y. purified proteins and performed PET degradation experiments. Hongzhao.W., Y.C., and M.W. performed PET degradation experiments in bioreactors. X.D., Hao.W. and Y.F. crystallized proteins and performed X-ray diffraction experiments and refinements. Hongzhao. W., J.Z., and P.W. performed computational design experiments. Y.Z., Hongzhao.W., and Y.F. wrote the manuscript. Y.Z. edited the manuscript. All authors have given their approval to the final version of the manuscript.

Competing interests

The authors declare no competing interests.

Additional information

Supplementary information The online version contains supplementary material available at <https://doi.org/10.1038/s42003-025-08364-6>.

Correspondence and requests for materials should be addressed to Yue Feng or Yushan Zhu.

Peer review information *Communications Biology* thanks the anonymous reviewers for their contribution to the peer review of this work. Primary Handling Editors: Aylin Bircan. A peer review file is available.

Reprints and permissions information is available at <http://www.nature.com/reprints>

Publisher's note Springer Nature remains neutral with regard to jurisdictional claims in published maps and institutional affiliations.

Open Access This article is licensed under a Creative Commons Attribution-NonCommercial-NoDerivatives 4.0 International License, which permits any non-commercial use, sharing, distribution and reproduction in any medium or format, as long as you give appropriate credit to the original author(s) and the source, provide a link to the Creative Commons licence, and indicate if you modified the licensed material. You do not have permission under this licence to share adapted material derived from this article or parts of it. The images or other third party material in this article are included in the article's Creative Commons licence, unless indicated otherwise in a credit line to the material. If material is not included in the article's Creative Commons licence and your intended use is not permitted by statutory regulation or exceeds the permitted use, you will need to obtain permission directly from the copyright holder. To view a copy of this licence, visit <http://creativecommons.org/licenses/by-nc-nd/4.0/>.

© The Author(s) 2025